DESIGN AND CHARACTERIZATION OF A MICRO MECHANICAL TEST DEVICE

A THESIS SUBMITTED TO

THE GRADUATE SCHOOL OF ENGINEERING AND SCIENCE

OF BILKENT UNIVERSITY

IN PARTIAL FULFILLMENT OF THE REQUIREMENTS FOR

THE DEGREE OF

MASTER OF SCIENCE

IN

MECHANICAL ENGINEERING

By

Elif Altıntepe

August 2016

DESIGN AND CHARACTERIZATION OF A MICRO MECHANICAL TEST DEVICE

By Elif Altıntepe

August 2016

We certify that we have read this thesis and that in our opinion it is fully adequate, in scope and in quality, as a thesis for the degree of Master of Science.

Adnan Akay(Advisor)

Onur Özcan

Özgür Ünver

Approved for the Graduate School of Engineering and Science:

Levent Onural
Director of the Graduate School

ABSTRACT

DESIGN AND CHARACTERIZATION OF A MICRO MECHANICAL TEST DEVICE

Elif Altıntepe
M.S. in Mechanical Engineering
Advisor: Adnan Akay
August 2016

Devices with micro- and nano- scale components are becoming more commonplace and demand for better quantification of the properties such as Young's modulus, stiffness, and damping of small-scale components is increasing. Since these properties can differ significantly from their bulk values, their direct measurements using a micro mechanical test device is offered in the thesis. The micro-scale test device described in this thesis consists of a platform that also includes subsystems to measure stress and strain, actuation, sample fabrication and grippers to mount the samples.

A notch-flexure based monolithic structure is used for the device platform to provide high-resolution precise motion. A piezoelectric actuator, a force transducer, and a vibrometer are used for actuation, force measurement and velocity measurement, respectively.

Finite element analyses and experiments are carried out in order to characterize the apparatus as a micro mechanical test device. Static, time-dependent cases are analyzed and its eigenfrequencies are determined. Required calibrations and drift analysis of instruments are conducted. Force and velocity relations are obtained, and results are evaluated for linearity and repeatability. Finally, operating range of proposed device is determined for use as a micro mechanical test device.

Keywords: Micro mechanical test device, circular hinge, monolithic structure, piezoelectric actuator.

ÖZET

MİKRO MEKANİK TEST CİHAZININ DİZAYNI VE KARAKTERİZASYONU

Elif Altıntepe
Makine Mühendisliği, Yüksek Lisans
Tez Danışmanı: Adnan Akay
Ağustos 2016

Mikro- ve nano- boyutlardaki komponentler içeren cihazların kullanımının artmasıyla, mikrometre boyutlarındaki malzemelerin elastisite modülü, sertlik ve sönümlenme oranı gibi özelliklerinin belirlenmesi önem taşımaktadır. Mikro boyutlarda malzemenin mekanik özelliklerinin aynı malzemenin büyük boyutlarından farklılaşması sebebiyle bu tezde malzeme özelliklerinin mikro çekme testi ile direkt olarak belirlenmesi önerilmektedir. Yüksek çözünürlükte gerilim ve gerinim ölçmek, hareketi sağlamak, numuneyi hazırlamak, test aletini ve numune tutucuları dizayn etmek çekme testinin önemli parçalarıdır. Bu tezin amacı mikrometre boyutlarındaki malzelemelerin özelliklerini belirlemeyebilmek için mikro mekanik test cihazını dizayn ve karakterize etmektir.

Çentikli bükülebilen yekpare yapı yüksek çözünürlükte ve hassas hareket sağlayabildiği için bu cihaz için uygundur. Piezoelektrik eyleyici, kuvvet transdüseri ve vibrometre sırasıyla hareketi sağlamak, kuvvet ölçmek ve hız ölçmek için kullanılmıştır.

Dizayn edilen cihazın mikro mekanik test cihazı olarak kullanılabilirliğini görmek için sonlu eleman analizleri ve deneyler yapıldı. Durağan, zamana bağlı ve doğal frekans analizleri yapıldı. Kullanılan cihazların gerekli kalibrasyonları ve kayma analizleri yapıldı. Deneysel olarak da kuvvet ve hız ilişkisi bulundu ve sonuçlar lineerlik ve tekrarlanabilirlik açısından incelendi. Son olarak, cihazın çalışma aralığı belirlendi ve önerilen dizaynın mikro mekanik test cihazı olarak kullanılabileceğine karar verildi.

Anahtar sözcükler: Mikro mekanik test cihazı, dairesel menteşe, yekpare yapı, piezoelektrik eyleyici.

Acknowledgement

Firstly, I would like to express profound gratitude to my thesis advisor Prof. Adnan Akay for continuous support for my study and for his patience and immense knowledge.

Besides my advisor, I would like to thank the rest of my thesis committee Assistant Prof. Onur Özcan and Assistant Prof. Özgür Ünver for their insightful comments.

I would also like to acknowledge Dr. Şakir Baytaroğlu, Dr. Samad Nadimi Bavil Oliaei and Mustafa Kılıç for their help and valuable knowledge.

I thank to my friends, Aylin Altaytaş, Semih Günerten, Başak Avcı, Neginsadat Musavi, Stefan Ristevski and Alper Tiftikçi for their support and for all the fun we have had in the last three years.

Finally, I thank to my mother, Filiz Altıntepe, and to my boyfriend, Talip Özakça, for their patience and their love. They provide me with unfailing support and continuous encouragement throughout my years of study. This accomplishment would not have been possible without them.

Contents

List of Figures

List of Tables

Chapter 1

Introduction

Microelectromechanical systems (MEMS) and nanoelectromechanical systems (NEMS) have become a significant research and application area. Despite the improvements of design and fabrication of MEMS, ambiguities exist in mechanical behavior of small sized materials [1]. Thus, mechanical testing techniques at these length scales play an important role. The motivation of this thesis is to develop a micro mechanical test system for characterizing micro-scale materials.

1.1 Overview of micro tensile test

Micro tensile testing is one of the important ways to determine mechanical properties such as yield strength, stiffness or Young's modulus of materials. Micro tensile test systems consist of subsystems: actuation, stress and strain measurement, specimen preparation, handling and gripping. As specimen dimensions decrease, the challenges of the tests increase, and each subsystem has its own challenges. High-resolution actuation as well as accurate measurement of stress and strain are required for micro tensile tests [1, 2].

Use of piezoelectric actuators is one of the options for actuation. The main advantages of the piezoelectric actuators are capability of high resolution motion, controllability and working at both direct current (DC) and alternative current (AC) [1–4]. Thermal actuation is another way to provide motion. Zhu and Espinosa [5] use the inclined free standing beams (V-shaped beams) for thermal actuation shown in Figure 1.1. When voltage is applied across these beams,

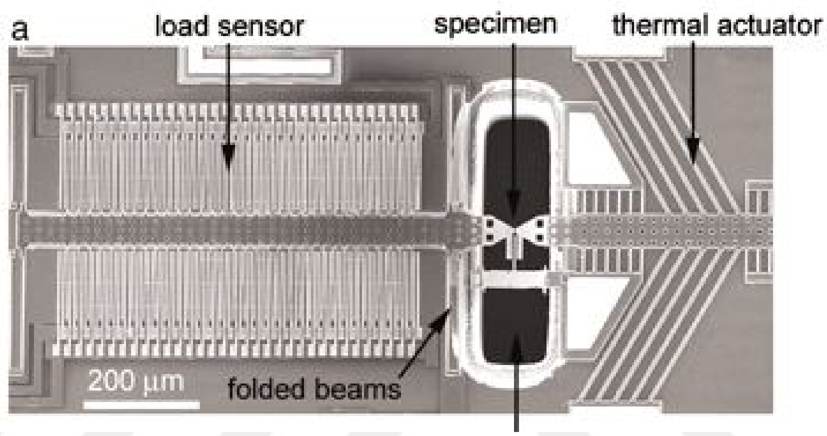

Figure 1.1: Example of thermal actuation [5]

thermal expansion occurs due to current flux, and the shuttle is pushed forward due to inclined configuration of the beams [5]. A magnet-coil force actuator can also be used in micro tensile test systems since it allows small displacements, linear operation, and low hysteresis. This system includes spring, permanent magnet, a magnetic coil and clamps for specimen [6]. The tensile force is applied by a magnetic coil force actuator and depends on the electric current in the magnet coil. The relationship between force and electric current is obtained by calibration [6, 7]. DC motors [8, 9] and inchworm actuators [10] are other alternatives for actuation in micro test systems.

Accurate measurement of force and displacement are other significant parts of the micro tensile test systems. There are various ways to measure small forces. One approach involves use of commercial load cells. Seguineau and his colleagues [8] use a miniature piezoresistive load cell. Another example has a load cell with temperature compensation and high load precision of 100 μN with the maximum load capacity of 180 N is used in their test system [9]. Furthermore, Chasiotis and Knauss [10] use miniature tension-comparison load cell to measure small forces on micron sized polysilicon thin films. The load cell's maximum capacity

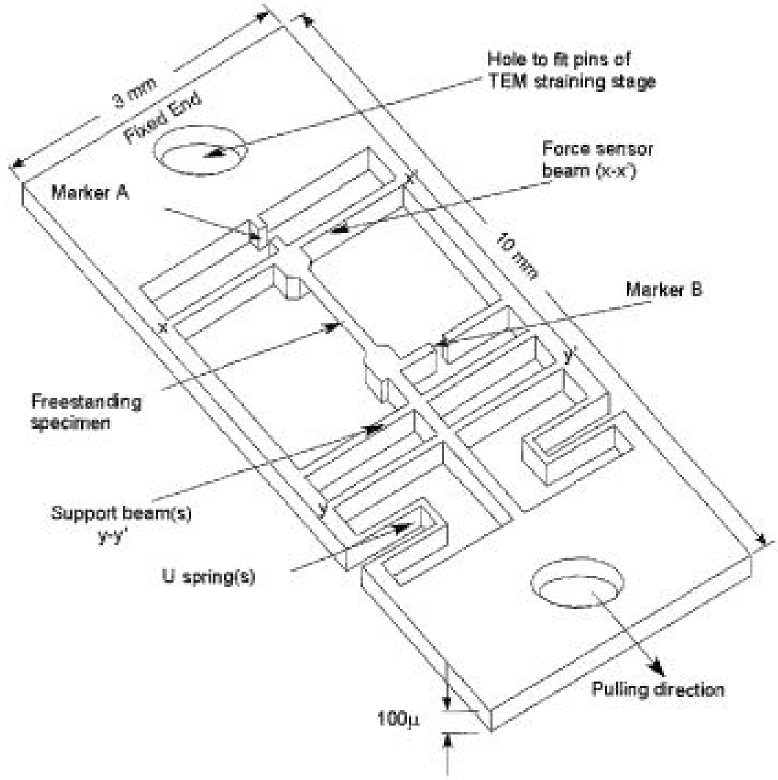

Figure 1.2: Force sensing beams [3]

is 0.5 N and its accuracy is 10^{-4} N [10]. Force on 600 μm wide and 3.5 μm thick phosphorus-doped polysilicon specimen is measured with load cell with resolution 5 mN and maximum load capacity 4.5 N [11]. Another approach involves a flexure-based system to measure loads, shown in Figure 1.2 [3]. Force on the sample is measured by force-sensing beams. The force depends on the transverse deflection of the beams and the spring constant of the beams. The resolution of the measured force is related to spring constant of the beams, and it depends on beam dimensions [1, 3, 12]. Additionally, the load sensor which can be seen in Figure 1.1 is based on differential capacitance measurements [5]. The load sensor includes a rigid shuttle with fixed and movable electrodes anchored to the specimen by folded beams. The change of the shuttle's displacement leads to capacitance change resulting in measured voltage change. Since the spring constant of the folded beams is known, the applied force is proportional to the measured voltage. Thus, this type of the load cell can be used to measure small forces [5,13].

There are different methods to determine the strain of small sized specimens. The most accurate results can be obtained when the strain is measured directly on the specimen. However, decreasing the specimen size makes this measurement difficult. Interferometric strain/displacement gage is one way to non-contact, direct strain measurement. Two reflective gage markers are placed on a specimen, and they are illuminated with a laser. Diffracted reflections results in fringe patterns which are captured by photosensors, and relative displacement of the markers is measured to obtain strain result [11]. Digital image correlation (DIC) is a more popular direct method that uses scanning electron microscope (SEM), transmission electron microscope (TEM), atomic force microscope (AFM) or high resolution camera to obtain strain information. Han et al. [12] obtain both stress strain data and images of the deforming samples from SEM images. Similarly, Haque and Saif [3] conduct their tests under TEM and SEM. Their design can fit in a TEM stage, and they obtain displacement data from SEM/TEM images. The advantage of this method is that it captures both full-field strain measurement and local shape change related to yielding and fracture [2]. However, DIC method is used for characterizing sub-micron materials, and the motion platform can fit in a microscope stage. Additionally, differential digital image tracking (DDIT) is technique to determine strain of the specimen. The camera tracks the markers on the specimen, and sequential digital images are saved. Post processing of the data is required to obtain strain measurement results that makes this method challenging [2,14]. Moreover, the displacement sensors such as inductive or capacitive sensors can be used to determine displacement of the specimen. However, the accuracy of the displacement results depends on the resolution of the sensors. If a displacement sensor is used, the dimensions of the specimen should be selected according to the sensor specifications. For instance, an inductive displacement sensor with 20 nm resolution is preferred to measure displacement of 1 mm wide, 1-5 μm thick, and 1-5 mm long thin films [15].

Besides the accurate measurement of force and displacement, handling, gripping and manipulating the micro- and nano- scale specimens are significant challenges

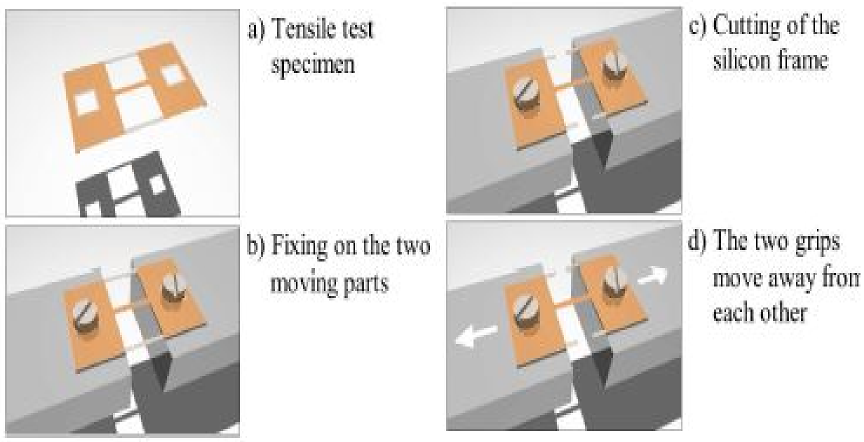

Figure 1.3: Specimen fixation [8]

due to their fragility. Thus, new techniques for handling and gripping have to be developed. One of prevailing methods involves manufacturing of specimen with a large support structure. Thus, the specimen can be handled by conventional tools such a support structure can be seen in Figure 1.3 [8]. After mounting of the specimen on the test system, the frame is cut to release the sample. Although a support frame makes the handling easy, removing them is also a tedious procedure. A small rotating diamond saw can be used to cut the frame. However, the saw causes excessive vibration which can damage the specimens. It is important that samples are fixed by grippers, so they become immobilized [9]. The holes on the support structure are used to mount the thin films to the test system easily. If the samples are micro-scale wires or fibers, the support structure and the gripper structure are changed slightly. Graph papers [16] or cardboards [17] can be used as support frame. The paper based support frames are similar to frame of thin films as shown in Figure 1.3. Using adhesives, the wires are attached to the papers which have a hole in the middle that can be seen in Figure 1.4 [16].

Another preferred method is the co-fabrication of the test system and the specimen. Zhu and Espinosa [5] have co-fabricated and performed tensile test of thin polysilicon films. Furthermore, Haque and Saif [3] prefer the co-fabrication of the specimen with test apparatus because it allows perfect alignment and gripping. The adhesion between the silicon substrate and the sample material plays a role as gripping, so an extra gripping mechanism is not needed [3].

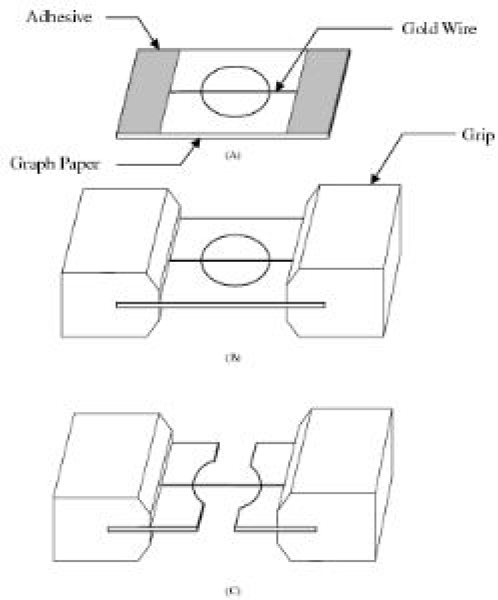

Figure 1.4: Micro wire gripping [16]

The specimen selection is one of the most important factors for micro tensile tests because test system and the specimen have mutual dynamic dependency. In other words, test apparatus is designed according to test sample, and the sample is selected according to test system specifications. Therefore, wide range of materials such as spider silk [18], biomaterials [17] or carbon nanotubes [5] can be tested by micro tensile test device. Moreover, the dimensions of samples become significant in order to get accurate results from the designed test system. The important aspect is that micro-scale materials can show different mechanical behavior than bulk materials. When size of the material decreases, its strength increases due to absence of defects in the material atomic structure [5].

When the micro tensile test apparatus and its components such as sensors or actuators are compatible with fatigue test specifications, the test device can function as micro-scale fatigue test system. For instance, Szczepanski et al. [19] adapted the micro tensile test system to micro fatigue test system in order to find out the mechanical properties of 20 μm titanium alloy. Their test system includes piezoelectric actuator, load cell, silicon gripper and controller. Cho and Hemker [20] conduct both tensile and fatigue tests of the micro nickel structures. The micro-scale fatigue test machine consist of voice coil actuator, linear slider and grippers and dynamic load cells. Additionally, Seguineau [8] and coworkers perform tensile and fatigue test on the same test bench.

As a result, micro-scale fatigue test subsystems are similar to that of micro tensile test system. Both test systems require accurate measurements of force and displacement and high-resolution actuation.

1.2 Overview of flexure hinges

A flexure hinge (flexures) as defined by Lobontinu, is "a thin member that provides the relative rotation between two adjacent rigid members through flexing (bending)" [21]. They have superior properties when they are compared to conventional rotational joints. Firstly, they are monolithic, and this feature allows design of the monolithic mechanisms. Those mechanisms can operate until they fail which means that they do not need to be repaired. Monolithic structure eliminates friction losses, hysteresis and need for lubrication [21]. Secondly, they are compact so they can be used in small-scale applications. Thirdly, they can be easily manufactured by technologies such as electro discharged machining (EDM), laser cutting or end-milling. Lastly, and the most important feature of the flexure hinges is that they allow high-resolution and smooth motion [21, 22]. Thus, mechanisms that consist of flexure hinges are preferred in micro-scale applications such as micro-positioning, micro-grippers and micro-sensors.

On the other hand, flexure hinges have drawbacks such as limited range of motion, sensitivity to temperature changes, and possible complexity of the deformation. The range of motion depends on permissible stresses and strains in the material. For instance, thinnest portion of notch type of hinges encounters high stress concentrations. Since the motion is related to deformation of flexure hinges, these elements should stay in elastic region of the material [22]. Furthermore, the dimensions of the flexures can change due to thermal expansion or contraction making them sensitive to temperature changes [21]. Additionally, center of rotation is not fixed with respect to links it connects. Therefore, they are subjected to imprecise motion referred to as axis drift or parasitic motion [21,22]. Lastly, pure rotation cannot be obtained due to complex deformation that can include bending, axial shearing or torsional loading [21]. Since they are compliant elements in all directions, they undergo low rotation and translation in all directions which makes the motion complex [22]. As a result, designing, modelling and controlling flexures and compliant mechanisms have become interesting research area. The important points of flexure designs are discussed in detail in Chapter 2.

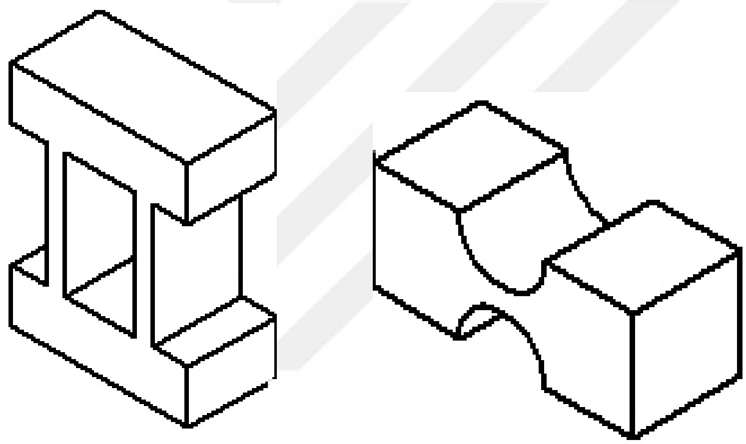

(a) Leaf type flexure hinge (b) Notch type flexure hinge

Figure 1.5: Flexure hinge types

The types of flexures can be divided into two main categories: notch type flexure hinges and leaf springs shown in Figure 1.5. Circular, corner filleted, elliptical, parabolic, hyperbolic flexure hinges are types of notch hinges. Leaf springs are simple beams. When leaf springs are compared to notch hinges, they have larger displacement ranges. However, they suffer from buckling under compressive loads and stiffening under the tensile loads [23]. Combination of flexures can lead to formation of new mechanisms such as micro-positioning stages, grippers or translational and revolute joints.

Parallel four-bar blocks (parallelogram) can form translational joints. They can involve leaf springs or notch hinges. A conventional parallelogram is shown in Figure 1.5a, and double parallelogram in Figure 1.6. [23].

Flexures can be used in gripper design that requires high positioning accuracy.

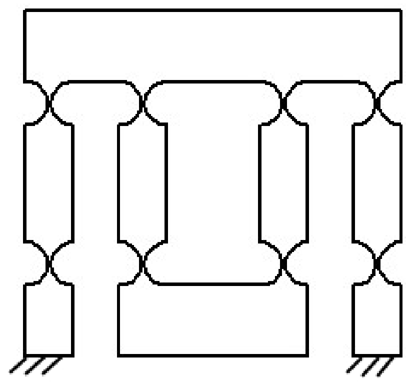

Figure 1.6: Double parallelogram

For example, Ai and Xu [24] design and analyze a compliant gripper for micro-manipulation and micro-assembly applications. The gripper includes a parallelogram to obtain pure translational motion as well as right circular hinges. They achieve pure translational motion with compact, compliant gripper design as shown in Figure 1.7 [24]. In a different example of micro-gripper design proposes use of an amplifier mechanism added to the flexure-based system. This amplifier also consists of flexures that points out another application area of flexure hinges. Both circular hinges and rectangular hinges are used to improve precision and allow good deformation, respectively [25]. Flexure hinges are frequently used in micro-positioning stages since they provide precise smooth motion. For instance, in a triangular planar motion platform designed for laser micro machining application. Motion platform is composed of one prismatic, two revolute joints, and these joints are replaced with corresponding flexure hinges. For these joints, conventional parallelogram is used as prismatic joint and circular hinge is used as revolute joints. [26].

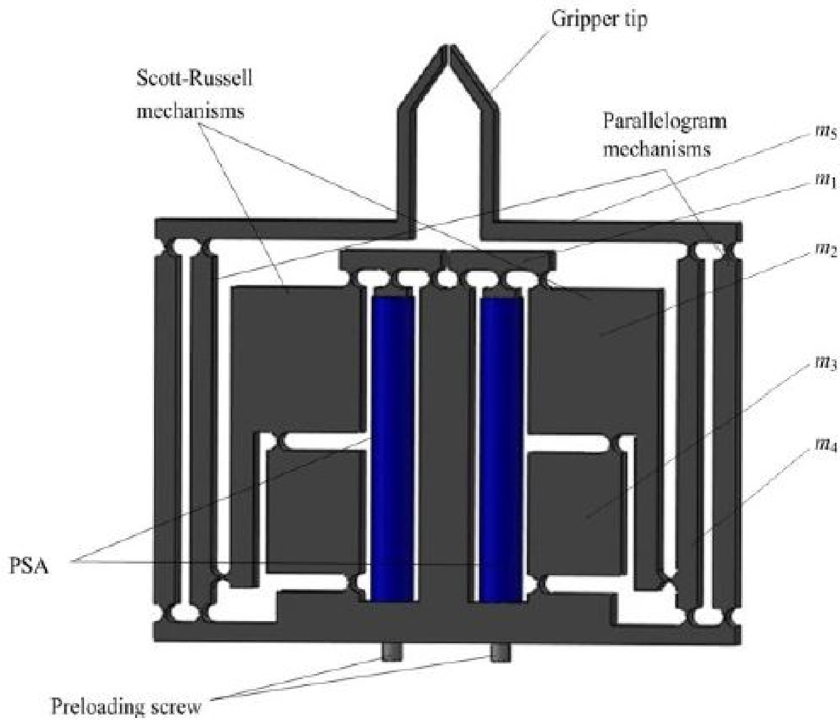

Figure 1.7: Compliant gripper [24]

Finally, a flexure based mechanism can be used as micro mechanical test machine. Gudlavalleti et al. [15] designed a micro tensile machine based on a leaf spring double parallelogram. The design consists of two compound flexures that are used for actuation and force measurement.

Therefore, the flexure hinges present a preferred design where high-resolution, frictionless and smooth motion is required. The aim of micro-positioning and micro tensile devices are similar in terms of providing precise, high-resolution motion. Therefore, a compliant micro tensile test apparatus can be designed by using flexure hinges which is the main focus of this thesis.

1.3 Thesis outline

The thesis can be divided into four main topics: design, finite element analysis (FEA) of the design, calibration of sensors, and system characterization. The current chapter presented an overview of micro tensile tests and flexure hinges.

Chapter 2 presents mechanical design of the device. Mechanical design includes a hinge-based moving platform and supporting parts for sensors such as force transducers, and capacitive displacement sensor. Since the main part of the design is based on hinges, the theory of hinge is also discussed in chapter 2 as well as the manufacturing process used to produce the device.

Chapter 3 discusses the finite element analyses of the prototypes. Comsol Multiphysics program is used for finite element simulations. Static, time-dependent, eigenfrequency analysis are conducted.

Chapter 4 introduces actuation and sensing elements of the system, and their calibrations. A piezoelectric actuator is used for actuation and force is measured by piezoelectric force transducer. Velocity and displacement are measured by vibrometer and capacitive sensors, respectively. Since properties of these elements are important to the system response, calibration of force transducer and capacitive sensor are also presented in this chapter.

Chapter 5 shows the system characterization results. The system response under various inputs, its repeatability, linearity and the resonance frequencies of the system are presented. FEA results and the measurement results are compared. Additionally, the sources of the uncertainties and the results are discussed.

Chapter 6 summarizes the major results, conclusions and the future work for the improvement of the system and its application.

Chapter 2

Mechanical Design

This chapter presents the design of a micro mechanical test device, which is based on flexure hinges. Firstly, theory of flexures and important factors for design procedure are discussed. Then, the design requirements and conceptual design are explained. Lastly, manufacturing process and final design are described.

2.1 Theory of circular hinges

The flexures in the present context can be divided into three main categories in terms of their functionality: single axis, multiple axis and two-axis. The sensitive axis, or the compliant axis, is defined as an axis about which limited relative rotation between adjacent links is produced. For instance, single axis flexures are sensitive to only rotation about one axis which is the sensitive axis. Circular hinges, corner-filleted, elliptical, parabolic, hyperbolic hinges belong to single axis flexure hinge group. Figure 2.1 shows a circular hinge sensitive axis that lies in the cross-section of minimum thickness where maximum bending occurs, and is perpendicular to the longitudinal and transverse axes [21].

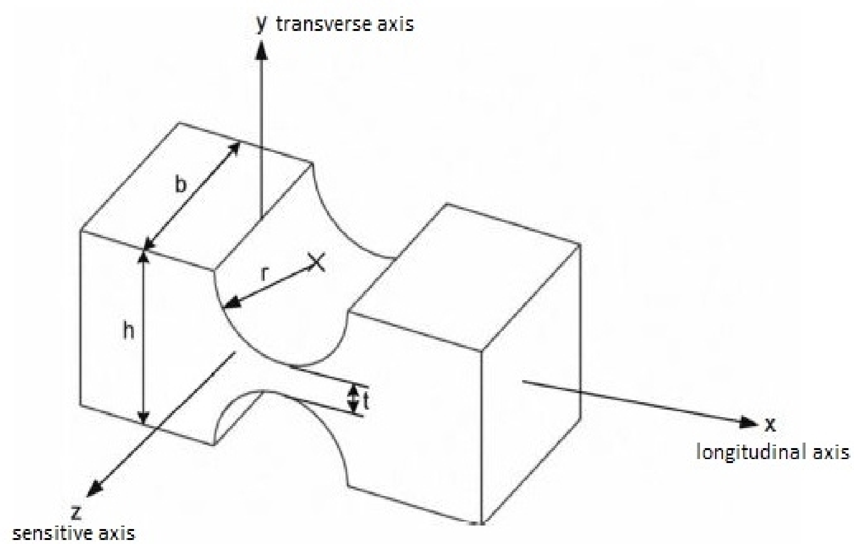

Figure 2.1: Circular hinge geometry and axes

Derivation of compliance equations of the hinges are useful for designing flexures. Compliance, inverse of stiffness, provide the relationships between force-displacement and moment-rotation, respectively. Furthermore, capacity of rotation, precision of rotation, stress levels, and sensitivity to parasitic loading can be understood by derived compliance equations, and these parameters should be considered at the design stage. Capacity of rotation is related to motion range and precision of rotation is related to displacement of rotation center where the geometric symmetry of the flexure is located [21]. There are various derived compliance equations but in this thesis Lobontiu's compliance equations for circular hinges are presented.

According to Lobontiu [21], reciprocity principle and Castigliano's displacement theorem are useful for deriving closed-form compliance equation. According to reciprocity principle, "the deformation produced at a location i by a unit load that is being applied at a different location j is equal to the deformation produced at location j by a unit load that acts at i" [21]. The compliance matrix can be expressed as the inverse of the stiffness matrix since as a result of reciprocity principle, the compliance matrix is square and symmetric [21]. Moreover, Castigliano's displacement theorem helps the calculation of deformations of elastic bodies under external loading and support reactions. However, this theorem is restricted to linearly elastic materials. According to Castigliano's theorem, linear displacement and angular deformation of an elastic body can be expressed in terms of partial derivative of total strain energy with respect to force and moment, respectively [21].

The important geometric parameters of circular hinges are the radius of circular hinge, r, the minimum thickness, t, the thickness, h, and the width of flexure, b. Figure 2.1 shows the circular hinge and all the important parameters. Besides the geometry, material properties become significant for design of flexures. The aim of the design is to make the hinge as compliant as possible in the desired direction, and stiff in other directions to decrease parasitic motion. Forces act in axial direction (F_x) and transverse direction (F_y) and the moment about sensitive axis (M_z) provide planar motion. However, moment about x and y axis (M_x, M_y), force acts to z axis (F_z) cause out of plane motion that are parasitic motions. In two dimensional applications, torsional effect (M_x) can be ignored as it is rare [21]. Lobontiu [21] derives these compliances as:

$$\begin{aligned}\frac{\alpha_z}{M_z} &= \frac{24r}{Ebt^3(2r+t)(4r+t)^3}[t(4r+t)(6r^2+4rt+t^2) \\ &\quad + 6r(2r+t^2)\sqrt{t(4r+t)}\arctan(\sqrt{1+\frac{4r}{t}})]\end{aligned} \tag{2.1}$$

$$\frac{\Delta_x}{F_x} = \frac{1}{Eb}[\frac{2(2r+t)}{\sqrt{t(4r+t)}}\arctan\sqrt{1+\frac{4r}{t}} - \frac{\pi}{2}] \tag{2.2}$$

$$\begin{aligned}\frac{\Delta_y}{F_y} &= \frac{3}{4Eb(2r+t)}[2r(2+\pi) + t\pi + \frac{8r^3(44r^2+28rt+5t^2)}{t^2(4r+t)^2} \\ &\quad + \frac{(2r+t)\sqrt{t(4r+t)}[-80r^4+24r^3t+8(3+2\pi)r^2t^2+4(1+2\pi)rt^3+t+t^4\pi]}{\sqrt{t^5(4r+t)^5}} \\ &\quad - \frac{8(2r+t)^4(-6r^2+4rt+t^2)}{\sqrt{t^5(4r+t)^5}}\arctan(\sqrt{1+\frac{4r}{t}})]\end{aligned} \tag{2.3}$$

The equations 2.1, 2.2 and 2.3 show the in-plane compliances, z, x, y directions respectively. E represents Young's modulus, and b, r, t are the geometric properties of the circular hinge described above. Thus, both material and geometric properties affect the compliances are given in the above equations. To better understand these relationships, compliances versus width, minimum thickness and radius are plotted. One parameter is changed while others are kept constant to obtain the effect of each parameter on compliances. Figure 2.2 shows the width effect on in-plane compliances, Figure 2.3 indicates relation between the minimum thickness and in-plane compliance and Figure 2.4 demonstrates the radius versus in-plane compliances. Result of the equations and plots show that increase in Young's modulus, width and minimum thickness decreases compliance whereas increase in radius leads to increase in compliances.

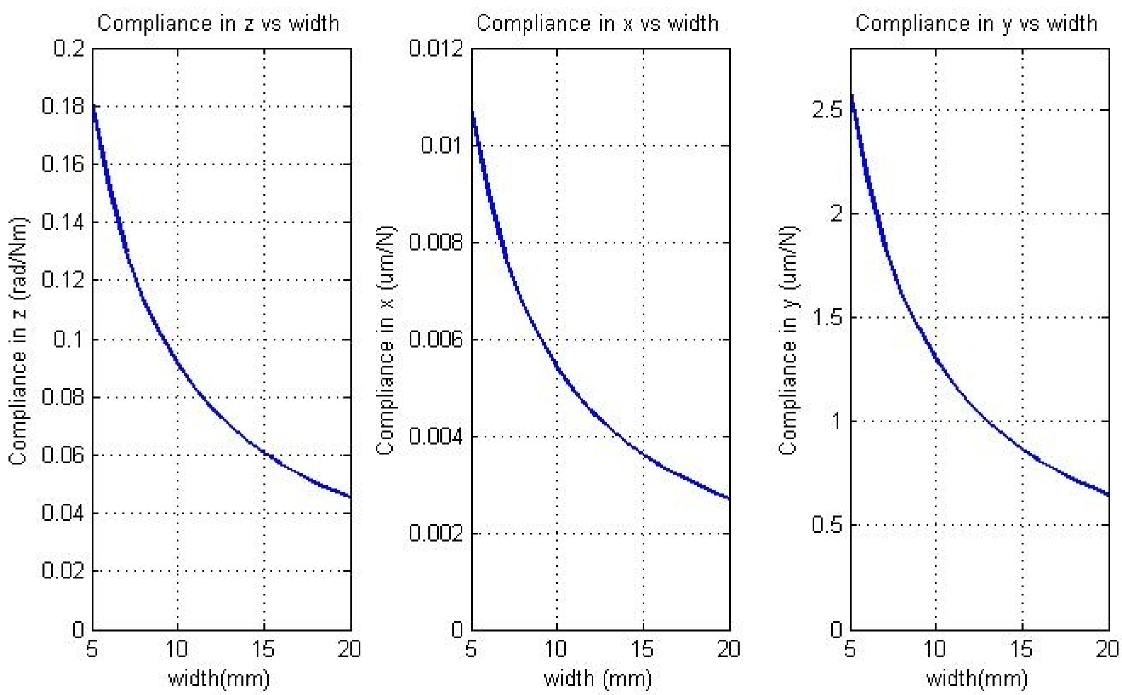

Figure 2.2: Compliance vs width

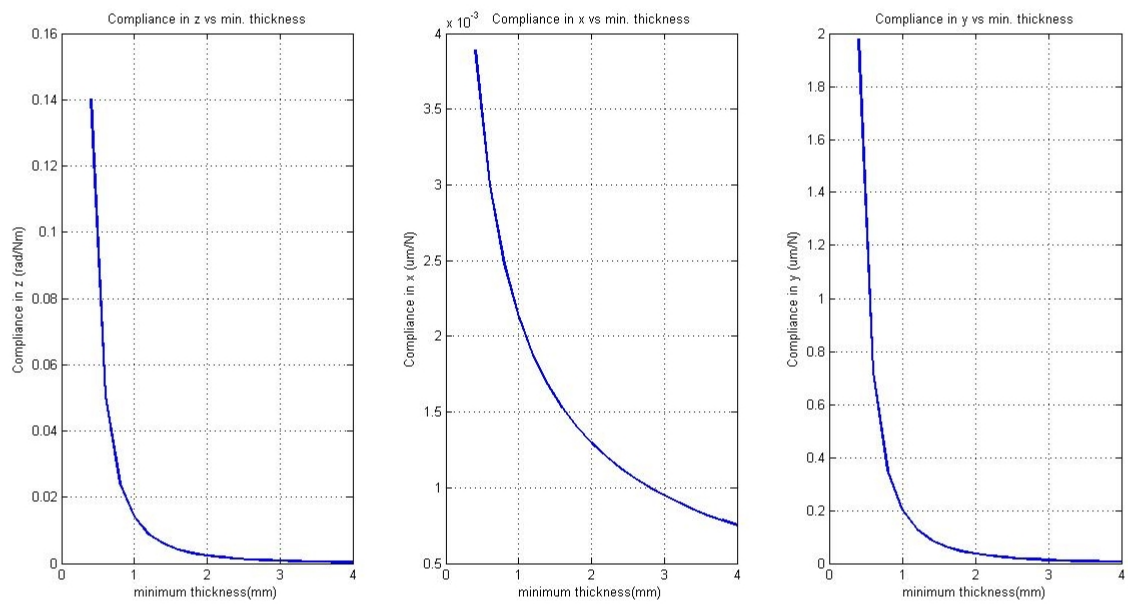

Figure 2.3: Compliance vs minimum thickness

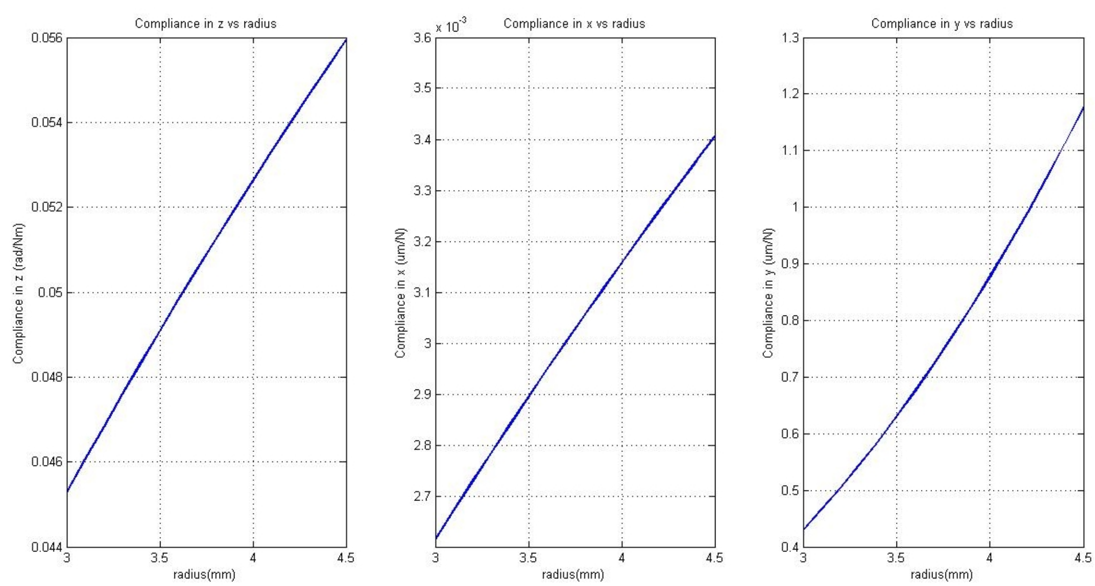

Figure 2.4: Compliance vs radius

2.2 Design specifications and conceptual design

Firstly, micro mechanical test stage should produce motion only in one direction to avoid misalignments. Besides the gripping mechanisms or erroneous installation of specimen that can cause misalignment problems, undesired motion of test stage can also result in misalignments. Thus, one of the requirements for design is to build a motion stage which moves only in one direction. Secondly, the device tests micro-scale materials with gage length equal and less than 1 mm. Therefore, one degree of freedom (DOF) translational flexure joint can be modified as a micro mechanical test device. As mentioned in Chapter 1, conventional parallelogram and double parallelogram are typical prismatic joints. However, main problem of the conventional parallelogram is having a limited motion range and presence of parasitic motions. On the other hand, double parallelogram in Figure 1.6 overcomes the conventional parallelogram problems with two mobile stages. However, it does not have uniform thermal expansion property because of its asymmetric structure [23]. This problem is solved by, Tang and Chen [23] with a large-displacement symmetric prismatic joint shown in Figure 2.5. This design can be regarded as a double parallelogram because it consists of one primary stages (shown in red) and two secondary motion stages (shown in green), and symmetric structure eliminates the axis drift. When the force along the Y axis is applied, secondary stages compensate the X axis motion, which results in elimination of axis drift and axial stress and increase the motion range with an increase in compliance in axial direction [23]. As a result, this joint can be altered as a micro mechanical test stage.

The proposed test system is actuated by a piezoelectric actuator, and the force transducer, vibrometer and capacitive displacement sensor are integrated to the system to measure force, velocity and displacement, respectively. Therefore, design includes necessary spaces for sensors and their supporting parts. Since the design is composed of circular hinges, it is manufactured by EDM. Brass or steel can be selected as material. When material properties are compared, yellow brass is selected due to having low Young's modulus and high yield strength. Table 2.1 shows the sensors and actuator dimensions. The stage is modified by taking

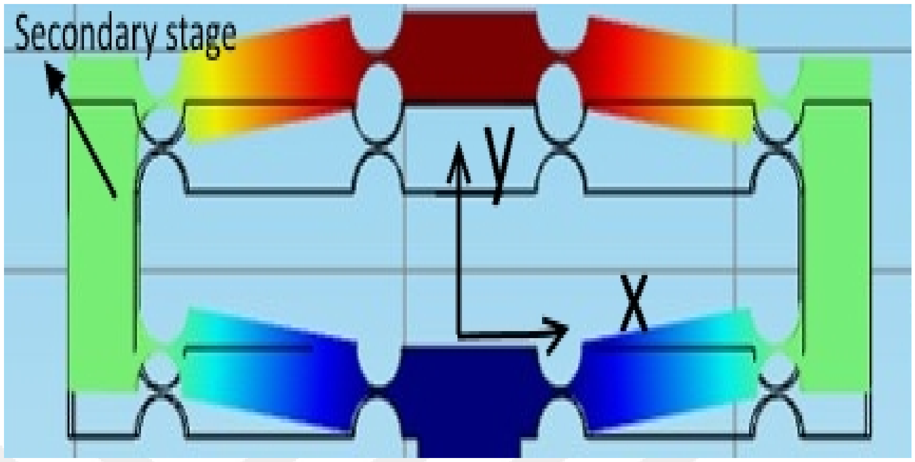

Figure 2.5: Large Displacement Prismatic Joint

Table 2.1: Dimensional requirements

Piezoelectric actuator dimension	10x10x36 mm
Force transducer dimension	11x10x11 mm
Laser linear reflector	30x37x38 mm
Capacitive sensor diameter	20 mm
Specimen gage length	<1mm

into consideration sensor and actuator dimensions and hinge geometry. Since PZT width is 10 mm and capacitive sensor diameter is 20 mm, the width of the circular hinges is selected as 18 mm. However, the compliance decreases by increase in width as mentioned before. Thus, dimensions of minimum thickness and radius are determined in order to increase the compliance of the hinge. The minimum thickness, t, is preferred to be less than 1 mm according to compliance graphs, Figure 2.3, and it is selected as 0.6 mm. Lastly, the radius of hinges is selected as 3.7 mm in order to keep design compact. The length of the primary stage is 38 mm because of the laser linear reflector. The conceptual design was drawn using SolidWorks and its final version presented below.

Figure 2.6 and Figure 2.7a and Figure 2.7b show dimetric, front and back views of the design, respectively. There is a frame around the stage in order to provide space for assembly of the sensors and mount the stage on rigid base, in this case an optical table. The underside of the design is shown where the piezoelectric actuator (PZT) is placed. One side of the PZT contacts the primary stage and enables its motion. The other side of the PZT contacts the force transducer. The connecting part is used between force transducer and PZT for assembling the force transducer. Lastly, when using a capacitive sensor, it is installed in the system via another support part similar to that of force transducer. If the capacitive sensor is not used, displacement or velocity can be measured from the primary stage directly without need for an extra piece to manufacture. The holes on both the primary stage and opposite surface can be used as the gripper, as mentioned in Chapter 1. The gripper is similar to Figure 1.4 and Figure 1.3. The assembly of the device can be seen in Figure 2.7c and Figure 2.7d. All detailed technical drawings can be found in Appendix A.

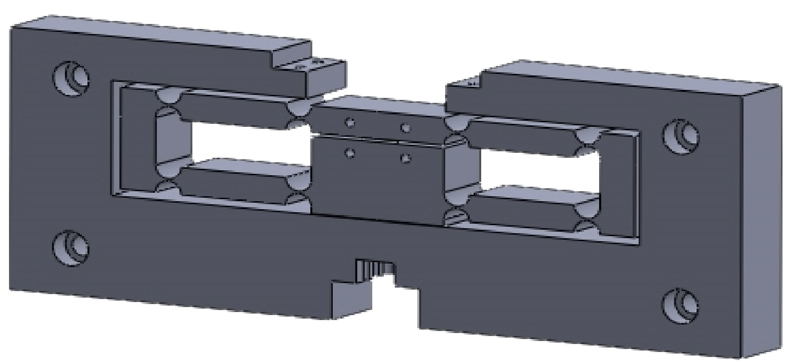

Figure 2.6: CAD drawing,dimetric view of stage

2.3 Manufacturing and overall test setup

In this section, manufacturing process and the manufactured and assembled design are presented. The material is yellow brass, UNS C27400 (MS63), and its Young's modulus is taken as 105 GPa and density is taken as 8470 kg/m^3 [27]. Firstly, the stage is manufactured by milling and EDM. PZT channel, force transducer and capacitive sensor spaces and all supports are prepared by milling. The inner shape of the stage is created also by milling machine. EDM is used for obtaining the final shape of the design. Figure 2.8 shows the EDM. Manufactured parts are presented in Figure 2.9 and assembled version of the device is

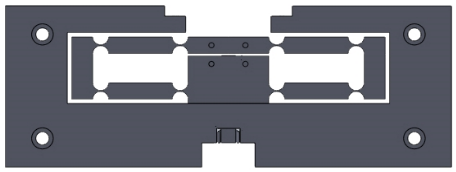

(a) CAD drawing,front view of stage

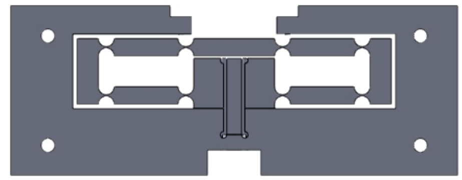

(b) CAD drawing,back view of stage

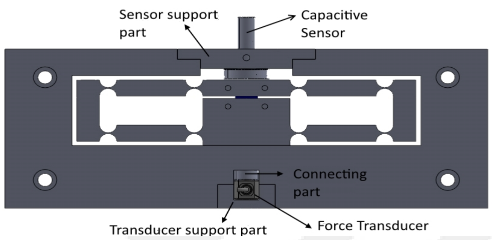

(c) CAD drawing,assembly of device, front view

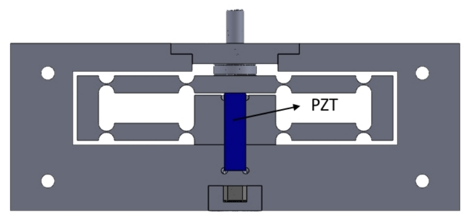

(d) CAD drawing, assembly of device, back view

Figure 2.7: CAD drawings

given in Figure 2.10. According to Figure 2.9, 1 shows the motion platform, 2 is piezoelectric actuator, 3 is force transducer, 4 is connecting part that is used with force transducer, 5 is support part for force transducer, 6 and 7 are also support parts for force transducer, not installed, 8 shows capacitive sensor and its support part, and 9 corresponds to bolts that are used for mounting.

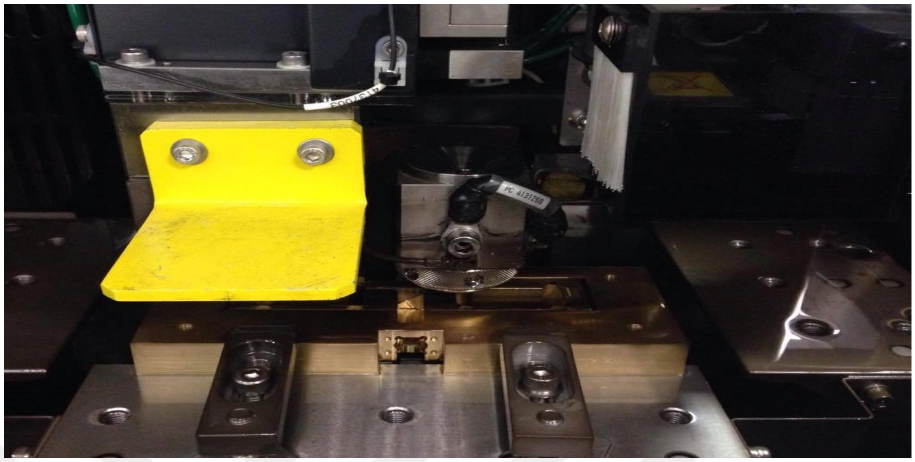

Figure 2.8: EDM

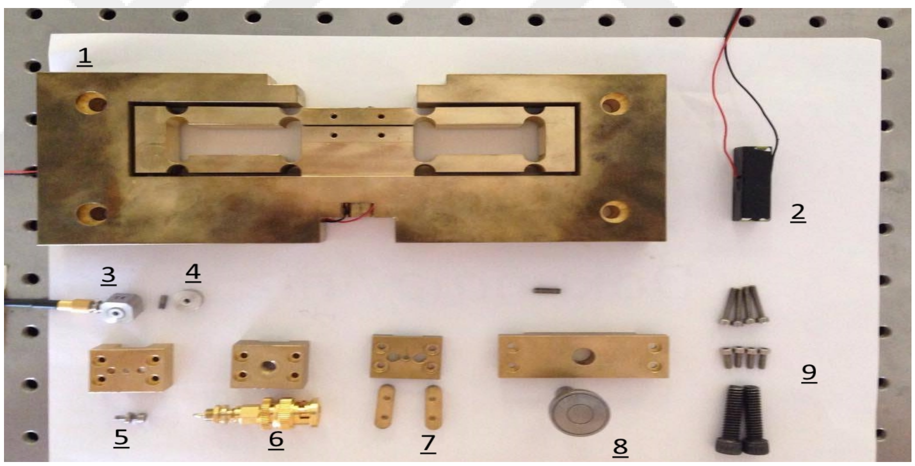

Figure 2.9: All parts of device

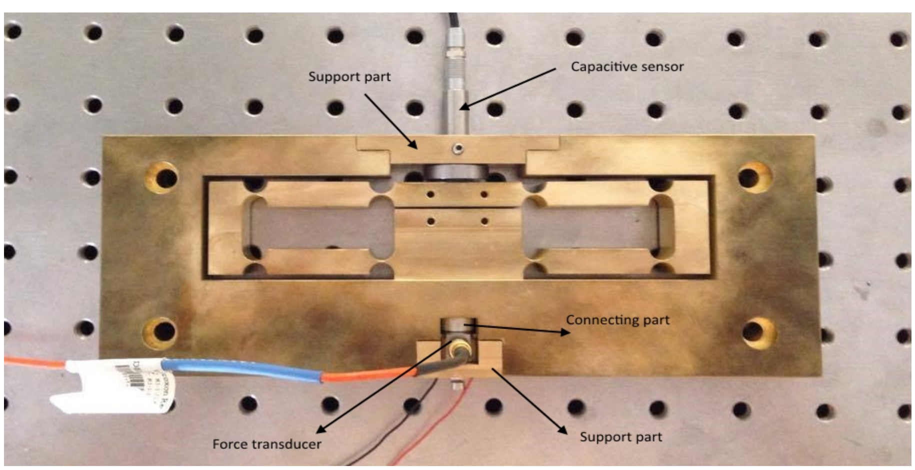

Figure 2.10: Assembled of the device

Chapter 3

Finite Element Analysis

The prototypes of the device are analyzed using a finite element method. Comsol Multiphysics is used for FEA. Static, time-dependent and eigenfrequency studies are conducted. Although the physics of the problem is not complicated, meshing of the geometry requires care. In this chapter, analysis results and important aspects related to mesh selection are discussed.

3.1 Static analysis

The model of the device is simulated for two different prototypes in order to understand the displacements in x, y, z directions of the primary stage. Motion only in one direction is expected because any motion in other directions cause misalignment of the specimen. Simulating prototypes can give an idea whether the selected design is suitable for micro mechanical test device. Hinge geometry and material properties remain the same for all models that are presented here. The different parameters examined are frame geometry, space for gage length, piezoelectric actuator place, the length of primary stage and features such as holes. Figure 3.1 shows the first and second prototypes of design.

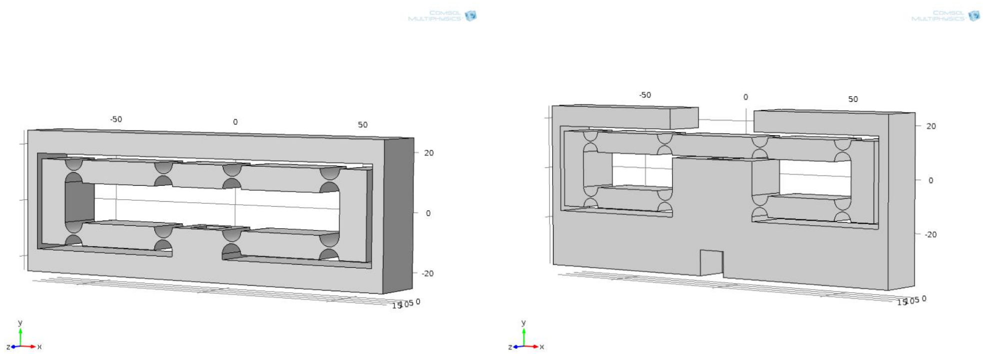

(a) prototype 1 (b) prototype 2

Figure 3.1: Simulated prototypes

The geometries are drawn in SolidWorks, and imported to Comsol, and material properties, boundary conditions and load are defined. Young's modulus (105 GPa), Poisson's ratio (0.34) and density (8470 kg/m^3) are used as material properties [27]. As boundary condition, fixed constraint is defined. Since the holes are not included, the side walls of the outer frame are fixed. In FEA programs, using symmetric boundary conditions decrease the computation time. However, it imposes fixed constraint at the out-of-symmetry plane direction and free in direction in-plane. Since the aim is to find x, y and z displacements of the center of primary stage, symmetric condition cannot be applied. Total force of 1 N is applied to primary stage surface where the actuator contacts. According to geometry configuration shown in Figure 3.1, force is applied along the +y direction. Total force is distributed on a boundary, in this case, 1 N is divided by the area of the surface that PZT contacts [28]. After defining boundary conditions, the geometry is meshed.

3.1.1 Meshing

The complicated geometry makes meshing a challenge. A circular hinge can cause rapid changes in geometry. Mesh subdivides the geometry and represents the solution field. Comsol offers two general options for meshing: physics and user controlled. The physics controlled mesh is not effective for this problem, so user controlled mesh that has predefined parameters is selected. Tetrahedral, hexahedra, prisms, and pyramid elements are types of mesh elements which are used in 3D problems. Tetrahedral is selected as mesh element type because it allows the meshing of any 3D geometry [29]. Mesh parameters are maximum and minimum element sizes, maximum element growth rate, curvature factor, resolution of narrow regions. Maximum and minimum element sizes limit how big and small each mesh element can be. Maximum growth rate determines the size differences of two adjacent mesh elements. Curvature factor controls the mesh element size along the curved boundary, and resolution of narrow regions determines the number of mesh elements in narrow regions. Lower value of maximum element size, minimum element size, maximum element growth rate and curvature factor lead to finer mesh, whereas higher value of resolution of narrow region allows better mesh [30]. Since the prioritization of parameters in the commercial software is not obvious, numerical experiments were carried out to determine the mesh algorithm shown below. Firstly, there is a hierarchy among the parameters. If the growth rate is 1 mm/mm and minimum and maximum elements sizes are equal, uniform mesh is obtained. Note that, growth rate should be equal or greater than one. Maximum element size, $h^{\max}$, and maximum growth rate should be determined as the first step of meshing. Resolution of curvature, h^c, minimum element size, $h^{\min}$, and resolution of narrow regions, h^n, are effective parameters to mesh.

Algorithm 1 Mesh Algorithm

```
h^c = max(h^min, h^c)
if h^c < h^n then
    h^c → h^n → h^max
else if h^n < h^c then
    h^n → h^min → h^max
end if
```

According to Mesh Algorithm if resolution of curvature is smaller than resolution of narrow region, resolution of curvature grows to resolution of narrow region then it grows to the maximum element size. In the second case, resolution of narrow region is smaller than resolution of curvature, resolution of narrow region grows to the minimum element size and then it grows to the maximum element size.

A small value for the resolution of curvature is selected and the minimum element size and resolution of the narrow region are compared. The mesh refinement is necessary to see convergence of results. Different values of mesh parameters are tried. However, mesh refinements have to be balanced with computational capabilities. For instance, when 1 mm is selected as the maximum element size, it creates too many elements, and problem solution takes unreasonably long.

Table 3.1: Displacement in y direction (μm) of center

		Minimum element size (mm)		
		0.2	0.3	0.4
	1.1	out of memory	out of memory	33.84468
growth	1.2	out of memory	33.90177	33.83191
rate	1.3	out of memory	33.8929	33.81963
	1.4	33.9181	33.88233	33.81068
	1.5	33.9143	33.87363	33.8035

Table 3.2: Displacement in x direction (nm) of center

		Minimum element size (mm)		
		0.2	0.3	0.4
	1.1	out of memory	out of memory	0.86957
growth	1.2	out of memory	0.0765	-0.95475
rate	1.3	out of memory	-0.01184	0.02917
	1.4	0.02125	-0.11855	0.29293
	1.5	-0.00649	0.03515	0.2498

Table 3.3: Displacement in z direction (nm) of center

		Minimum element size (mm)		
		0.2	0.3	0.4
	1.1	out of memory	out of memory	0.03509
growth	1.2	out of memory	-0.00483	-0.03104
rate	1.3	out of memory	-0.01956	0.00755
	1.4	0.0055	-0.02346	-0.01818
	1.5	-0.00922	-0.03232	0.07991

Table 3.1-3.3 indicate the y, x and z displacements of the first prototype center point (see Figure 3.2b and 3.2d), respectively. The maximum element size is 1.5

mm, resolution of curvature is 0.0001 mm/mm and the narrow region has one element. The growth rate and minimum element size are changed to obtain convergence. y direction corresponds to applied force direction, so x and z directions can cause parasitic motion. According to the above mesh results, displacements in x and z direction are less than 1 nm, suggesting negligible undesired motion in those directions.

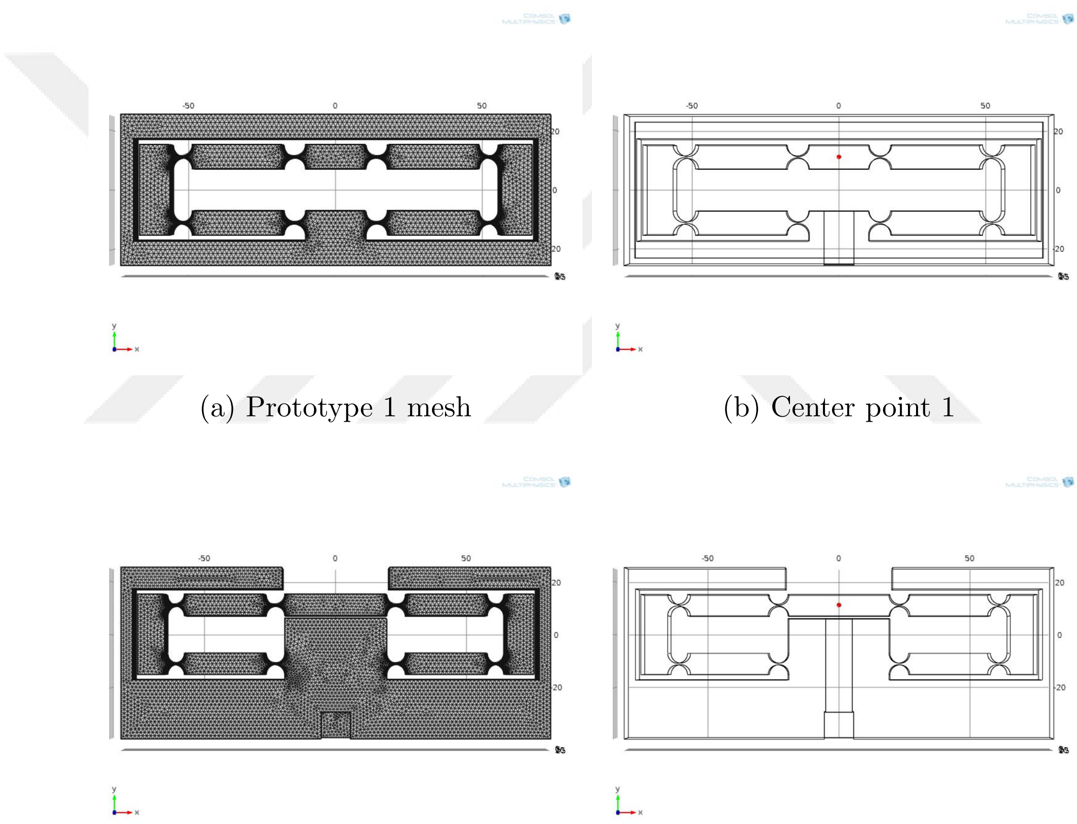

(a) Prototype 1 mesh

(b) Center point 1

(c) Prototype 2 mesh

(d) Center point 2

Figure 3.2: Meshed prototypes and center point

The second prototype is also meshed to see the effect of geometry difference on the results. The mesh parameters are selected as 1.5 mm maximum element size, 0.2 mm minimum element size, 1.5 mm/mm maximum element growth rate, 0.0001 mm/mm resolution of curvature and one element for resolution of narrow. Displacement of the same point (center) in y direction is 33.965 μm, x direction is -0.00843 nm and z direction is -0.1277 nm. When these results are compared with those for the first prototype, they are found to be close to. x and z displacements are still less than 1 nm and y displacement difference is approximately 23 nm, corresponding to a % 0.15 difference. Consequently, change in geometry does not have a serious effect on displacement results in static analysis.

In conclusion, two prototypes for the device are analyzed. Meshing algorithm helped to determine mesh parameters in order to obtain convergence. The first important outcome is that change of geometry does not affect the displacement results. The second important result is that the selected translational joint is suitable for a micro mechanical test device because there is no parasitic motion according to FEA results.

3.2 Time dependent analysis

Time dependent analyses of both prototypes are carried out. The boundary conditions and mesh are the same as those for static analysis. An isotropic loss factor of 5 10^{-4} is added because damping properties become important in the transient analysis. The most significant parameters in computations are sampling frequency and time steps of the solver. Increasing the sampling frequency leads to improved results. Even when a better sampling frequency is selected, time stepping methods are still important for Comsol. There are four options for generalized alpha (default) method: free, intermediate, manual and strict. In free-time stepping, time steps are chosen freely, in intermediate method, taking at least one step in each time subinterval is forced. The manual time stepping obeys the manually given time steps, and strict method can take additional steps in between given time steps as necessary [28]. The fastest and most accurate time stepping for this case is the manual method. Time steps are determined according to frequencies. A 10 Hz sinusoidal input is given to the surface where PZT actuator contacts. The amplitude of the input is 1 N. The sampling frequency is 200 Hz, so time steps are 5 msec. The results of center point are shown below in Figure 3.3.

Figure 3.4 indicates the displacement results of the second prototype. Since time-dependent analysis takes longer than static analysis, for the second prototype, the maximum element growth rate is changed from 1.5 mm/mm to 1.6 mm/mm and sampling frequency is reduced to 100 Hz. y displacement is consistent with static analysis results. The amplitude of the output is approximately 34 μm. Furthermore, x and z displacements are too small to be significant. In both cases, they are less than 1 nm. The transient response can be observed for the first 500 msec as a result of the damping factor used.

Based on time-dependent analyses, the change of geometry does not affect displacement results. The important outcome is that x and z displacements are less than 1 nm and, thus, are negligible for sinusoidal input.

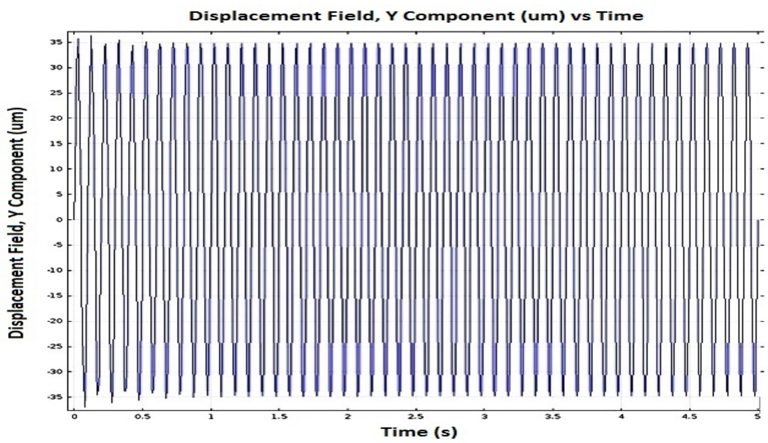

(a) Y displacement

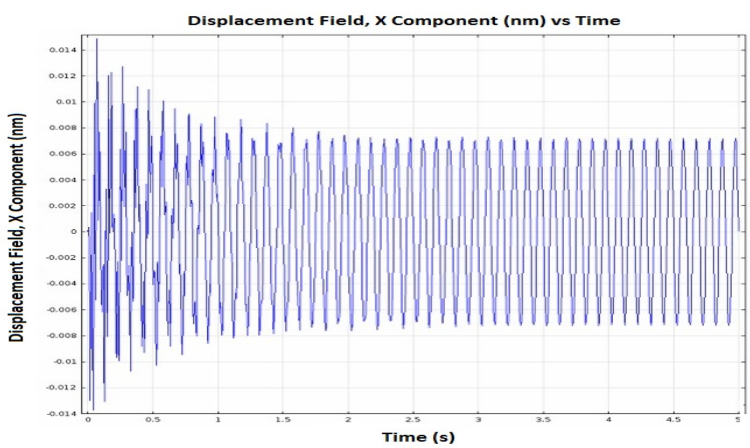

(b) X displacement

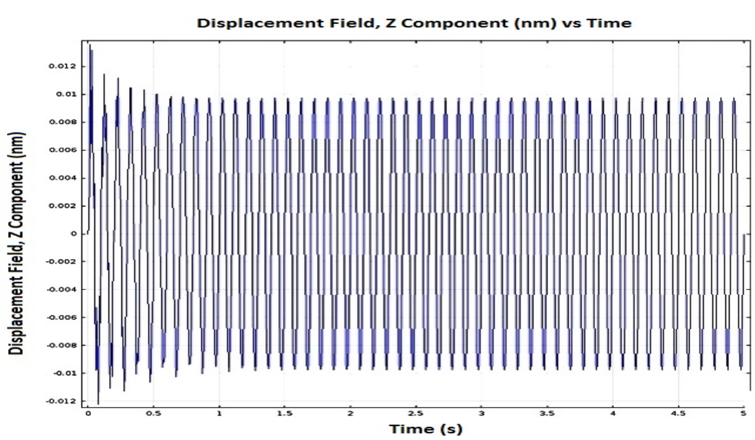

(c) Z displacement

Figure 3.3: Displacement response of center point 1 in x, y, z directions

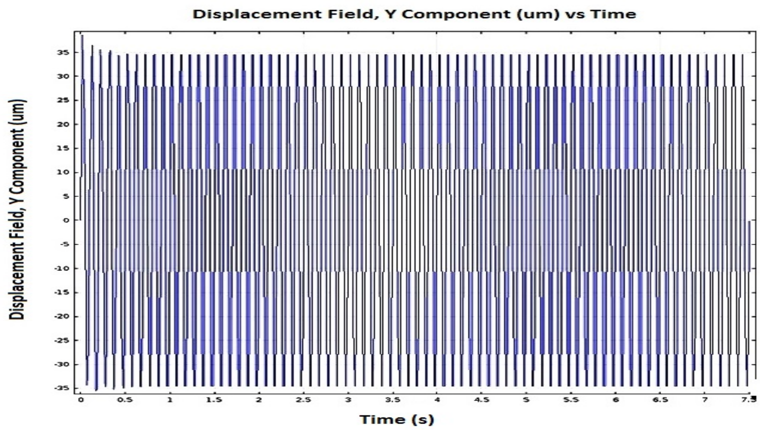

(a) Y displacement

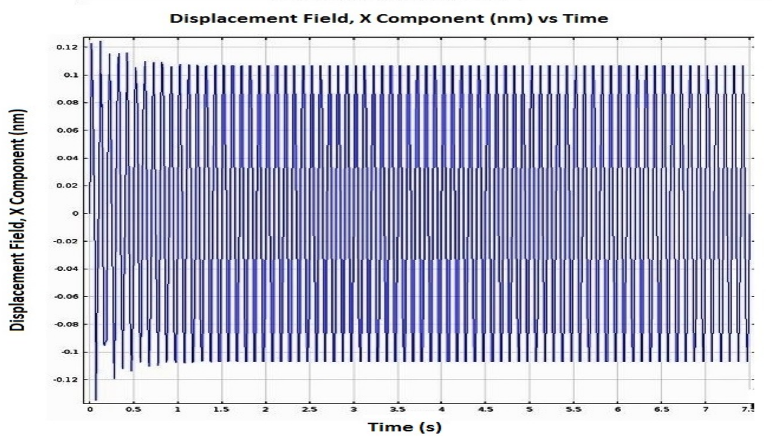

(b) X displacement

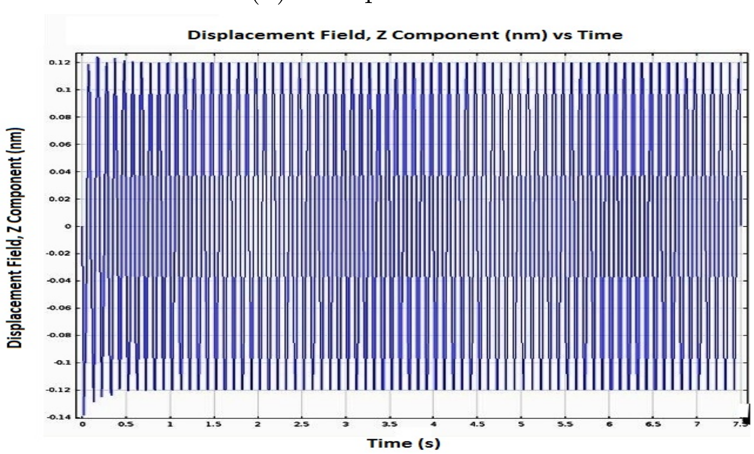

(c) Z displacement

Figure 3.4: Displacement response of center point 2 in x, y, z directions

3.3 Eigenfrequency analysis

Eigenfrequency analysis is carried out in order to find the natural frequencies and mode shapes of the device, which are important in measuring sample properties. Analyses are made to determine the working range of device. The first four natural frequencies are obtained.

Final version of design is simulated but outer frame and details like holes or channel of actuator that result in more elements at given mesh parameters above. Since model is symmetric, half model is meshed and solved using symmetry condition. Mesh parameters are changed in order to decrease the computational time and eliminate the possibility of running out of memory. New values for mesh parameters are selected using the mesh algorithm. Similar to the previous analyses, resolution of curvature is kept small at 0.0001 mm/mm, and the narrow region has only one element. The maximum element size is 2.5 mm and kept constant for different meshes. Various growth rates and minimum element sizes are tried to obtain convergence. Results are presented in Table 3.4. Figure 3.5 show the model that is meshed by minimum element size 0.3 mm with a growth rate 1.4 mm/mm.

According to Figures 3.6 -3.9, the second and fourth mode shapes are more important than others because they are in the direction of actuation. Furthermore, eigenfrequencies are converged to the results given in Table 3.4.

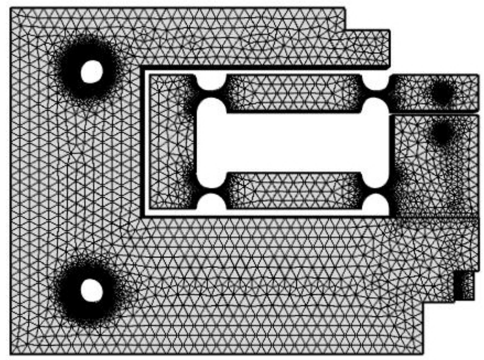

Figure 3.5: Meshed model

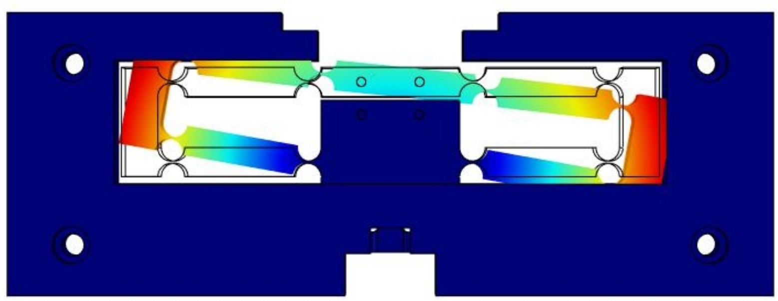

Figure 3.6: First mode shape

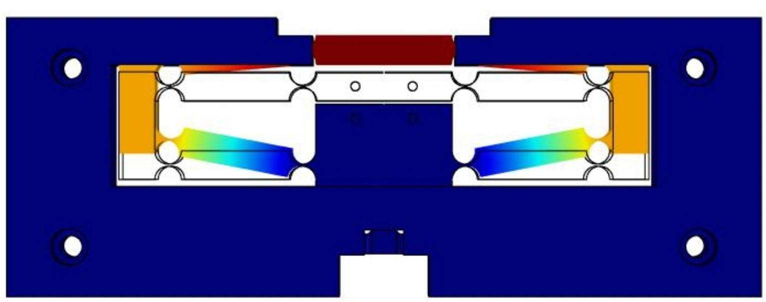

Figure 3.7: Second mode shape

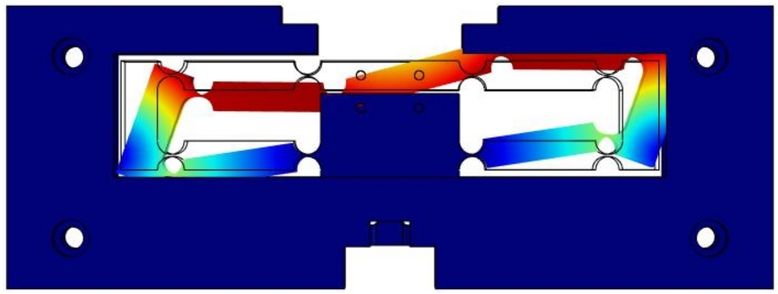

Figure 3.8: Third mode shape

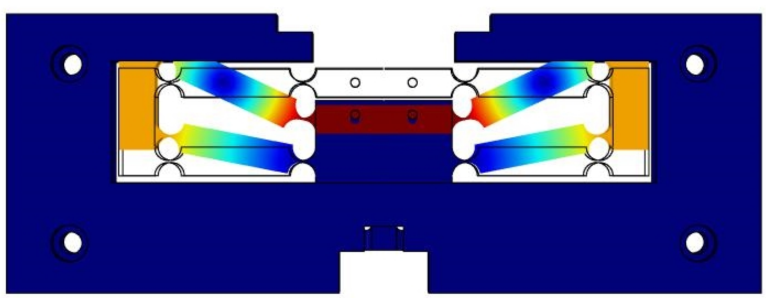

Figure 3.9: Fourth mode shape

Table 3.4: Eigenfrequency

		Natural Frequency (Hz)			
		First	Second	Third	Fourth
Mesh Parameters	Extra Fine	57.514	73.13	186.37	203.01
	Min: 0.4 mm Growth: 1.7	56.371	72.691	182.88	201.72
	Min: 0.4 mm Growth: 1.6	56.362	72.683	182.86	201.69
	Min: 0.4 mm Growth: 1.4	56.338	72.65	182.79	201.61
	Min: 0.4 mm Growth: 1.2	56.317	72.625	182.72	201.55
	Min: 0.3 mm Growth: 1.7	56.304	72.61	182.68	201.5
	Min: 0.3 mm Growth: 1.6	56.29	72.594	182.64	201.45
	Min: 0.3 mm Growth: 1.4	56.27	72.573	182.59	201.4

Chapter 4

Instruments and calibration

In this chapter, instruments that are used in test setup are introduced. Since, the system is actuated by a piezoelectric actuator, its working mechanism, advantages and disadvantages of PZT actuators are discussed. Important properties of force transducer, measurement results of force transducer, and its calibration are also explained and working mechanism of the capacitive displacement sensor, and its calibration results are presented. Lastly, properties of the vibrometer used are reviewed briefly.

4.1 Piezoelectric actuator

Piezoelectric effect is the ability of accumulation of electric charge in a crystal or ceramic in a response to applied pressure. The significant feature of this effect is its reversibility, which means that applying electric field to the crystal leads to deformation of the material. Actuators are based on this phenomenon are highly preferred in various application fields such as micro-electronics, measurement technology or precision mechanics [31].

Having sub-nanometer (theoretically infinitely small) position resolution is an important characteristics of PZT actuators. High-resolution of PZT is related to motion through solid state crystal effects. However, the resolution can be limited by piezo amplifiers used or mechanical factors such as mounting actuator or preload [31]. Furthermore, PZT actuators can work with both DC and AC conditions. Moreover, they can resist high loads and can generate high forces. Additionally, they have fast response time due to having high acceleration rates. Besides these advantages, they are compatible with vacuum, clean room or cryogenic temperatures [31–33].

Although PZT actuators have considerable advantages, they suffer from hysteresis and drift during open loop operations where the displacement corresponds to the drive voltage. Hysteresis results from crystalline polarization effects and molecular friction. As the applied voltage is increased and decreased, the hysteresis curve can be seen clearly, as voltage-stroke characteristics of an open loop PZT [31, 32]. Drift is another problem of open loop PZT. It is described as slow variation of displacement under constant applied voltage. It is related to remanent polarization. When the operating voltage is changed, the remanent polarization continues to change, so slow drift is observed after the voltage change is complete. Drift response has a logarithmic shape over time and equation 4.1 describes the drift as [34]:

$$L(t) = L_o[1 + \gamma \log_{10}(\frac{t}{0.1})] \tag{4.1}$$

Where L(t) is the displacement for any fixed input voltage, t is the time, γ is the drift factor which depends on the properties of PZT actuator, and L_o is the displacement 0.1 second after applying the input voltage [34]. Drift is a problem in DC applications, which is important for this project. To eliminate the hysteresis and drift, position sensor can be integrated to the system in order to measure displacement of the actuator, so voltage or current of the actuator is controlled. Therefore, close loop PZT actuators can provide more precise motion under constant applied voltage.

Besides the hysteresis and drift, self heating can be another disadvantage of PZT actuator. During a dynamic operation, heat is generated in the actuator, which is described as self heating. Internal friction of the moving piezo ceramic structure causes dissipation of electrical energy into heat. Amplitude and the frequency of the input are important parameters for self heating. Overheating can cause severe damage such as depoling in the PZT. Therefore, the operating frequency and input amplitude should be determined by considering self heating problem [32].

Understanding the relationship between force and stroke can be helpful to interpret working mechanism of the actuator. Generally, a PZT actuator is coupled with an external mechanism. However, when there is no coupled mechanism with PZT, it reaches the maximum stroke at maximum applied voltage. In this condition (stiffness of mechanism is zero) actuator does not generate a force. On the other hand, when PZT actuator motion is restricted, so that it cannot expand, it generates the maximum force at maximum applied voltage. Since it cannot expand, the resultant stroke is zero. When the constraining mechanism stiffness is finite, the PZT actuator stroke and generated force are reduced when compared to the extreme cases. Therefore, stiffness of the mechanism is important when producing force and stroke [31–33]

The PZT actuator is used in this project is a piezo stack actuator. American Piezo Ceramics Pst 150/10x10/40 is used and its specification is given in Table 4.1 [35]. Two maximum stroke values are given because there are different activation types such as unipolar activation and semi-bipolar activation. In unipolar activation, piezo actuator works in the voltage range from 0 to Vmax. In this case, maximum allowable voltage is 150 V and maximum achievable stroke is 40 μm. Furthermore, in semi-bipolar activation, the voltage range is increased $-V_{\min}$ to $V_{\max}$ in order to increase the stroke of the actuator. PZT material can operate with a %20 counter voltage of the specified maximum voltage. Consequently, piezo actuator used here can operate between -30 V and 150 V, with a corresponding stroke of 56 μm [32].

To avoid damaging the PZT actuator, it is important to apply correct voltage polarity within the range and use a suitable piezo amplifier are significant. American Piezo Ceramics SVR 150/3 PZT amplifier is used as actuator amplifier. It provides DC voltage to the actuator with a function generator is connected to

Table 4.1: Piezoactuator specifications

Max. stroke (μ)	56/40
Capacitance (nF)	7200
Resonance Frequency (kHz)	50
Stiffnes (N/μm)	250
Max load force (N)	8000
Blocking Force (N)	7000

the amplifier. Gain of the amplifier and offset can be arranged in order to apply both DC and AC signals. The function generator used is GW Instek SFG 2004.

4.2 Force transducer

A CFT 5 kN piezoelectric force transducer by Hottinger Baldwin Messtechnik GmbH (HBM), its analog amplifier CMA39 and QuantumX 840B data acquisition (DAQ) are used for measuring forces. Since force transducer has small dimensions, is supported by the transducer electronic data sheet (TEDS) and can easily mounted to the system, it is used in this project. [36]. The results are measured by force transducer are presented below and the main problems related to force measuring system and improvements are discussed.

Piezoelectric force transducers are preferred for dynamic applications. When force is applied to a piezoelectric force transducer, the quartz crystal generates electrostatic charges that dissipate. Applying dynamic forces does not allow the dissipation because electrostatic charges are generated rapidly and cannot dissipate rapidly, which explains the reason of using them in dynamic conditions [37].

AC voltage is applied to the PZT actuator, and force, displacement and velocity outcomes are measured when both AC and DC voltages are applied to the actuator, different force, displacement and velocity results are expected since DC voltage has a preload effect on the system. However, piezoelectric force transducers better perform under dynamic conditions, and the one used here has a drift, the induced value of preload is uncertain.

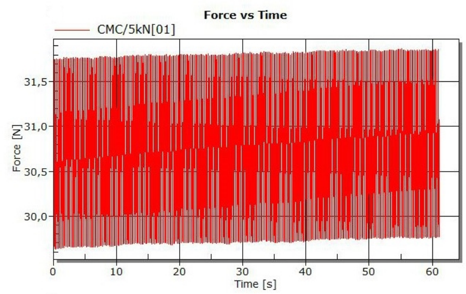

(a) Force(N)

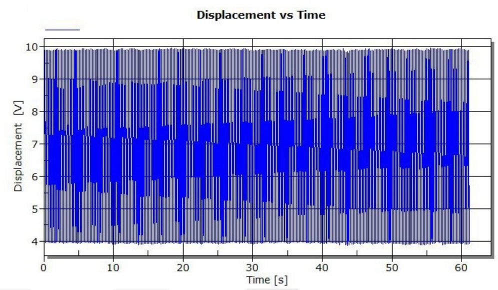

(b) Displacement (V)

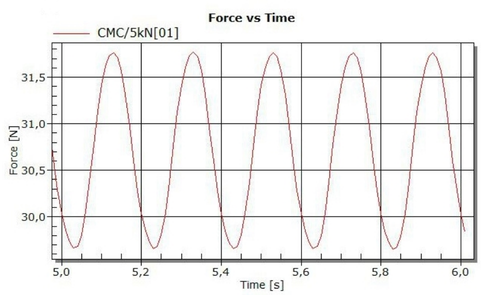

(c) Force graph,zoomed version

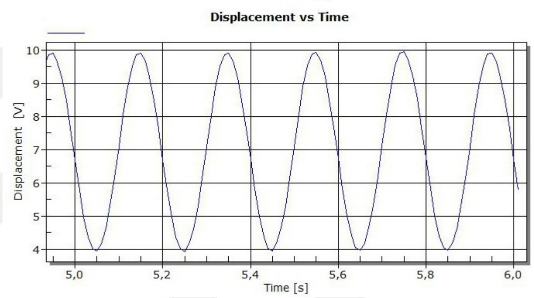

(d) Displacement graph,zoomed version

Figure 4.1: Force and displacement at 0 V DC

Figure 4.1 shows an example of force and displacement results. The displacement is measured by vibrometer and its sensitivity is 1 μm/V. Only AC sine wave with amplitude 16.2 V given as input, the drift of the force transducer can be seen in the Figure 4.1a. In contrast displacement graph, Figure 4.1b does not show drift.

From a separate measurement, Figure 4.2 shows results of a series of experiments where DC voltage levels are changed from 0 V to 50 V while the data are recorded. The transition parts are obvious, and they consists of overshoots that are the characteristic of piezo actuators. The drift is also observed.

Note that the initial value of the force, for this case approximately 26 N, is different than Figure 4.1a (30 N). This initial value depends on the force transducer charge amplifier characteristics, and changes day to day. The reasons can be related to discharging of the charge amplifier. According to measurement results,

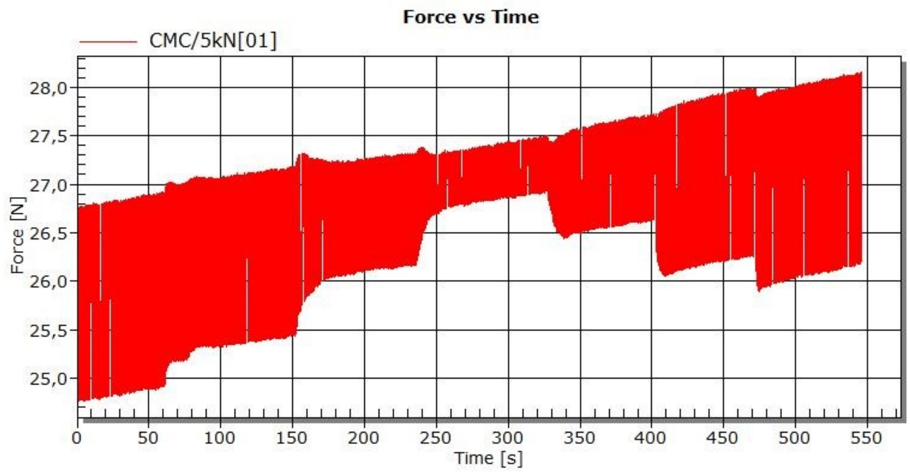

Figure 4.2: All data are included in a continuous experiment series

there is a drift that can cause misleading results. Since it is desirable to avoid having drift in measurements, it is important to determine parameters that affect drift, and thus force drift analysis are conducted.

4.2.1 Force drift analyses

This part describes the experiments carried out to investigate which parameters affect drift. Drift is change of DC force per minute and calculated here during the first minute of the measurements. It is important to determine the drift characteristics of the device to establish an input range for the test system. Since voltage is a controlled parameter in this system, its amplitude, frequency and DC voltage level of input are changed one at a time, and their effect on the drift is examined.

a) Amplitude Change

Both AC and DC voltages are applied to the piezo actuator as input voltage. The amplitude of AC input signal is changed during the experiment while data are saved continuously. This process is repeated for different DC (mean) voltages such as 0 V, 30 V, -10 V and -20 V. The frequency employed is 5 Hz, and the sampling frequency is 100 Hz. The results are represented below.

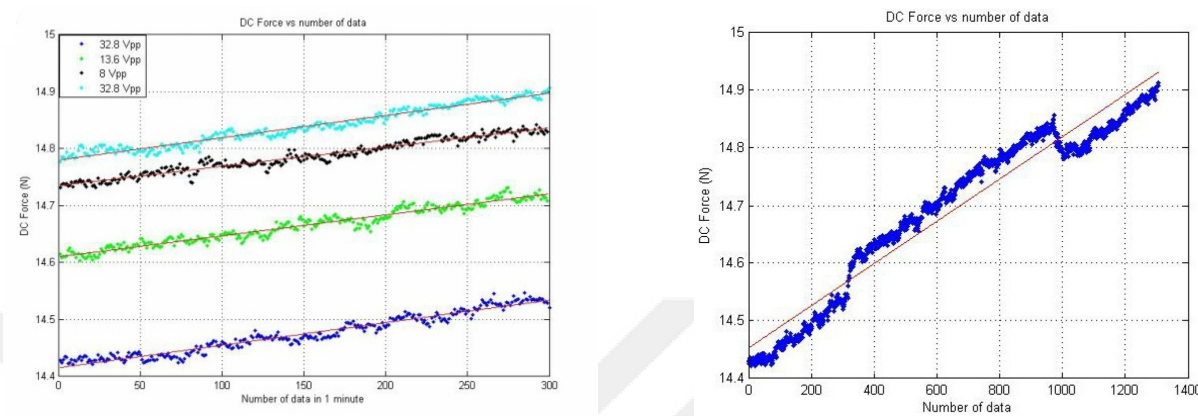

(a) Each case shown separately (b) All data shown

Figure 4.3: DC force at different amplitudes and 0V DC input

Table 4.2: The drift with respect to amplitude at 0 DC volt

Amplitude (V)	Drift (N/min)
16.4	0.11
6.8	0.11
4	0.1
16.4	0.12

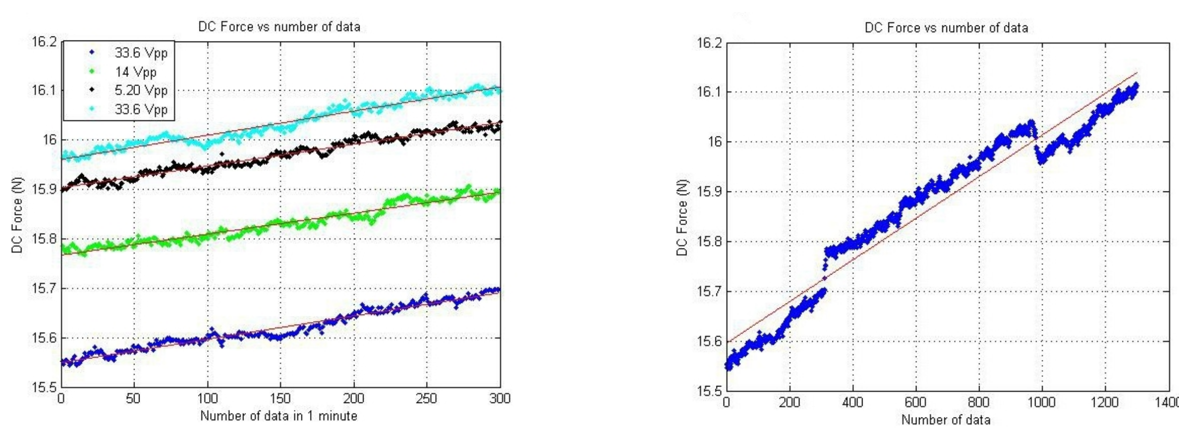

(a) Each case shown separately (b) All data shown

Figure 4.4: DC force at different amplitudes and 30V DC input

Table 4.3: The drift with respect to amplitude at 30 DC volt

Amplitude (V)	Drift (N/min)
16.8	0.14
7	0.12
2.6	0.14
16.8	0.15

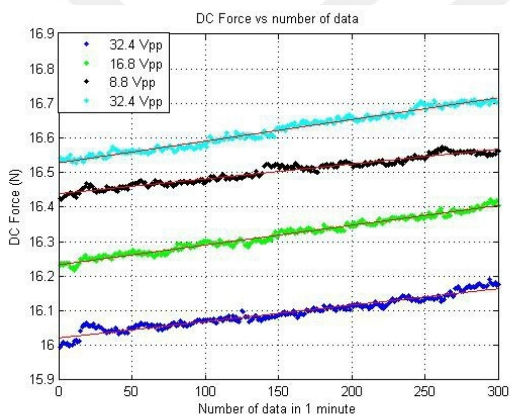

(a) Each case shown separately

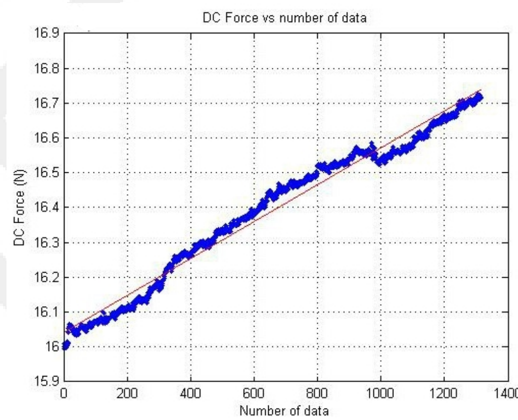

(b) All data shown

Figure 4.5: DC force at different amplitudes and -10V DC input

Table 4.4: The drift with respect to amplitude at -10 DC volt

Amplitude (V)	Drift (N/min)
16.2	0.14
8.4	0.17
4.4	0.13
16.2	0.18

Table 4.5: The drift with respect to amplitude at -20 DC volt

Amplitude (V)	Drift (N/min)
10	0.2
5.2	0.18
10.2	0.16

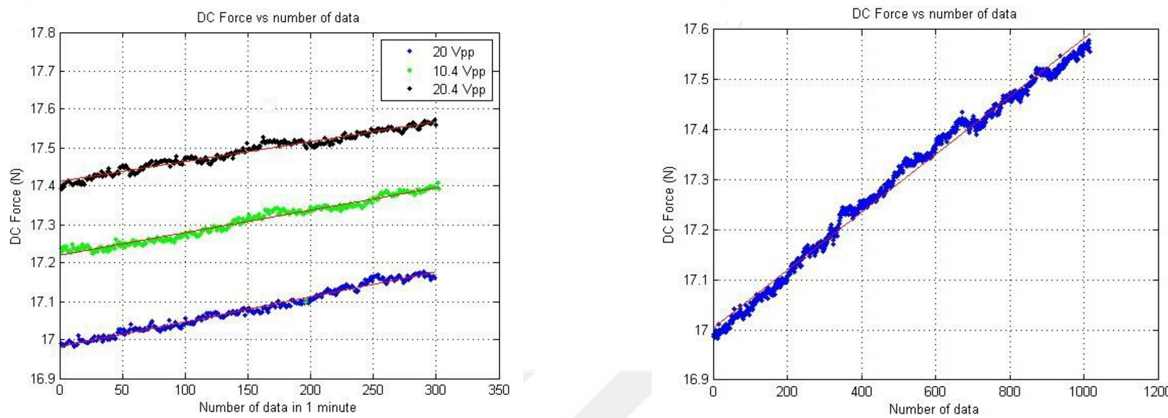

(a) Each case shown separately (b) All data shown

Figure 4.6: DC force at different amplitudes and -20V DC input

Figures 4.3- 4.6 show results of the experiments are conducted in order of 0 V_{DC}, 30 V_{DC}, -10 V_{DC}, -20 V_{DC}. Tables 4.2-4.5 list drift with respect to amplitudes for each DC voltage. In Figures 4.3a displays DC offset of force response one minute periods in response to different AC voltage amplitudes applied to the actuator. In this case has zero offset (0 V DC) applied voltage. In Figures 4.4a-4.6a similar results are shown but different values of DC offset associated with applied AC voltage to the actuator. In Figures 4.3b- 4.6b show the combined plots in Figures 4.3a-4.6a, respectively as they were obtained continuously. The experiments started with high amplitude, then amplitude is decreased, and again amplitude is increased to the initial value. When all data cases are examined, change of DC force levels are observed as a result of decrease in amplitude.

According to Tables 4.2- 4.5, drift of the system does not change with respect to amplitude of the input at different DC voltage levels. The critical outcome of these experiments is that change in amplitude affects the DC force level of the system. Since frequency is low, decrease in the amplitude results in increase in the DC force level which can be seen from Figures 4.3b-4.6b. In other words, low amplitudes behave as DC at low frequencies which leads to increase in DC level of force.

DC voltage has another important effect on DC force. Lower amplitude does not change DC force level at low DC voltage, Figure 4.5b and 4.6b. Therefore, system behaves similar to high frequency case. In other words, at low preload AC part becomes dominant. However, drawback of applying low DC voltage is the limitation of voltage range. When voltage becomes smaller than -30 V the input and the output are clipped. Although change in amplitude does not affect force drift, significant outcomes which indicate the relationship among the amplitude change, DC force level, and preload (DC voltage) are obtained.

b) DC voltage and frequency change

In this part, tests are performed at different DC voltage levels at 5 Hz and 40 Hz, respectively. 0, 10, 30, and 50 DC volts with constant AC signal cases are repeated. Relation between DC voltage and drift is discussed below. Then same experiments are repeated at 40 Hz to understand the frequency effect on system.

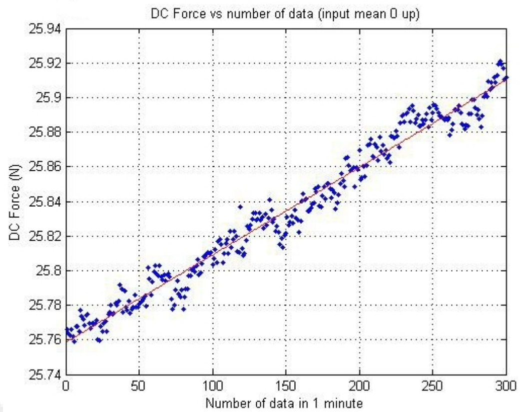

(a) 0 DC Voltage

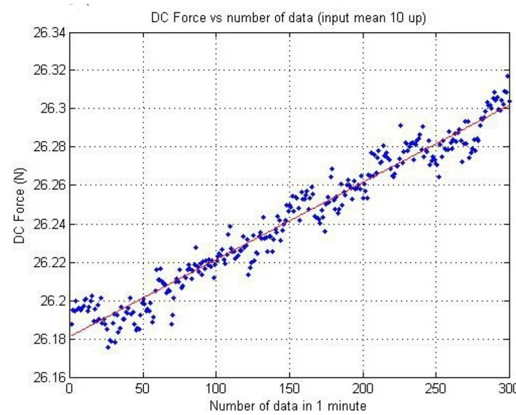

(b) 10 DC Voltage

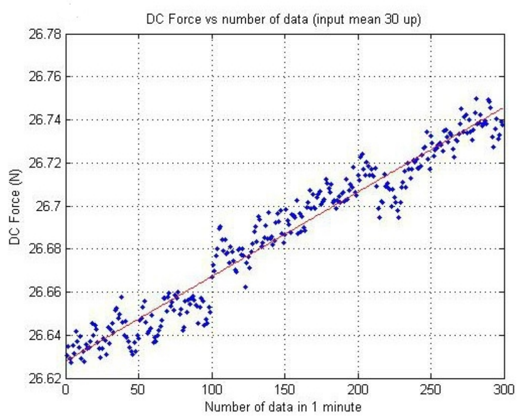

(c) 30 DC Voltage

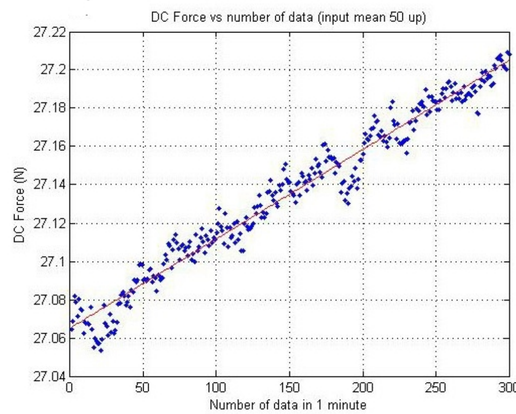

(d) 50 DC Voltage

Figure 4.7: DC force vs number of data in 1 minute at 5Hz

Table 4.6: Input voltage vs Drift at 5Hz

Input (V)	Drift (N/min)
0 V + 16.4sin(2πft)	0.15
10 V + 16.6sin(2πft)	0.12
30 V + 16.8sin(2πft)	0.12
50 V + 17.4sin(2πft)	0.14

Figure 4.7 and Table 4.6 indicate DC force drift with respect to different DC input voltage values with constant amplitudes at 5 Hz. Although piezo actuator gain and input are kept constant, some distortions of the sine wave amplitude are

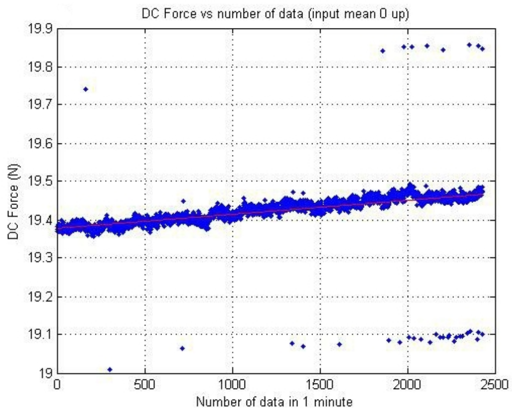

(a) 0 DC Voltage

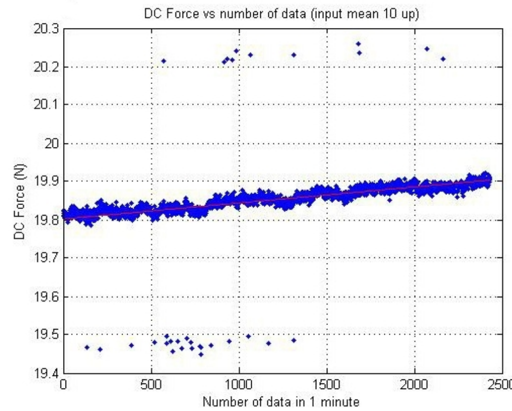

(b) 10 DC Voltage

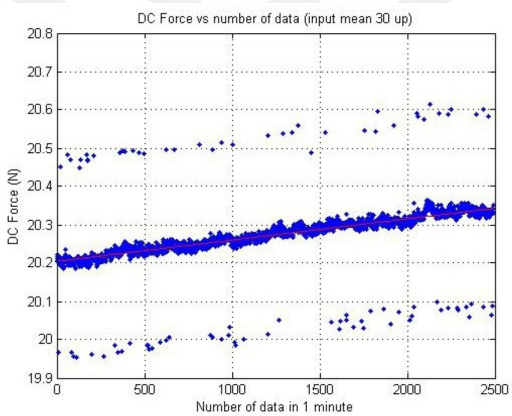

(c) 30 DC Voltage

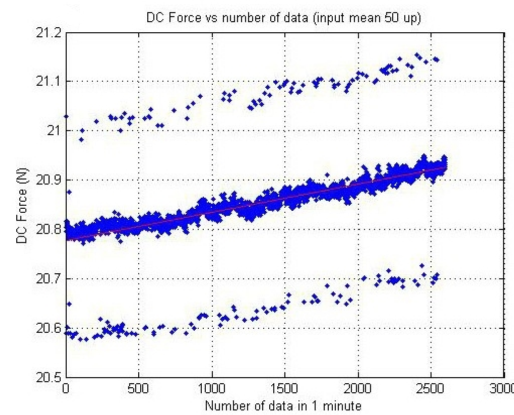

(d) 50 DC Voltage

Figure 4.8: DC force vs number of data in 1 minute at 40Hz

Table 4.7: Input voltage vs Drift at 40 Hz

Input (V)	Drift (N/min)
0 V + 5.4sin(2πft)	0.0888
10 V + 5.4sin(2πft)	0.1016
30 V + 6.2sin(2πft)	0.1381
50 V + 6.2sin(2πft)	0.1488

observed. Similar to previous results, drift varies between 0.11 N/min and 0.16 N/min.

Furthermore, Figure 4.8 and Table 4.7 show force drift in one minute at 40 Hz. Increasing input frequency results in distortions of force outputs. Since force data is noisier at high frequencies, DC force results show offset values above and below DC force that can be seen in Figure 4.8c and 4.8d (upper and lower dots). The noise is not considered at the drift calculation. The drift at 40 Hz is between 0.088 N/min and 0.15 N/min.

Measurements indicate that drift is less than 0.2 N/min, and is independent of frequency, amplitude and DC level of the input voltage. However, time is an important parameter for drift when the measurement sequence is considered. For instance, different amplitudes at -20 V DC measurements give the maximum drift is and the last measurement in that sequence.

HBM charge amplifier is known to exhibit drift and HBM company states that the maximum drift is 25 mN/sec which equals to 1.5 N/min [38]. This value does not change according to measured force, there are errors caused by drift if small forces are measured for a long time [39].

The measured drift is much less than stated maximum drift value. However, because the measured force values are small the results become unreliable because of drift. Thus, improvements described below are necessary to measure low force values accurately. Next section discusses the improvements.

4.2.2 Force transducer calibration

Force transducer used with charge amplifier is changed from HBM to Brüel & Kjaer (B&K) with high pass filter. Calibration of force transducer with B&K charge amplifier is required. For calibration, an accelerometer, Dytran 3035B1G, vibration exciter, DAQ, HBM force transducer and HBM charge amplifier and B&K charge amplifier are used. Force transducer is connected to HBM charge amplifier and is placed on the vibration exciter that provides motion. A known mass also is placed on top of the force transducer, and an accelerometer is placed on the mass. Using the B&K charge amplifier measurements are repeated at the same input voltage. Force transducer is calibrated at 40 Hz. Sensitivity of the force transducer with B&K charge amplifier is determined. Figure 4.9 and 4.10 show the force vs acceleration graphs with both charge amplifiers. The sensitivity of accelerometer is 1 mV/m/s^2. Force transducer with HBM amplifier is compared to force calculated from accelerometer and mass. Measured force is 4.618 N and calculated force is 4.643 N. The results are close to each other. The sensitivity of the force transducer with B&K amplifier is 1.263± 0.001 N/V. Sensitivity value is important because B&K charge amplifier with high pass filter is used for further experiments. As a result, drift is not observed by B&K amplifier with high pass filter which is a significant improvement.

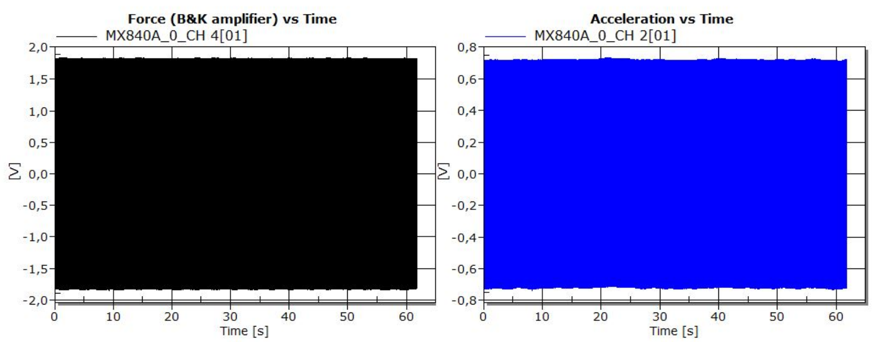

(a) Force and Acceleration Graphs (V)

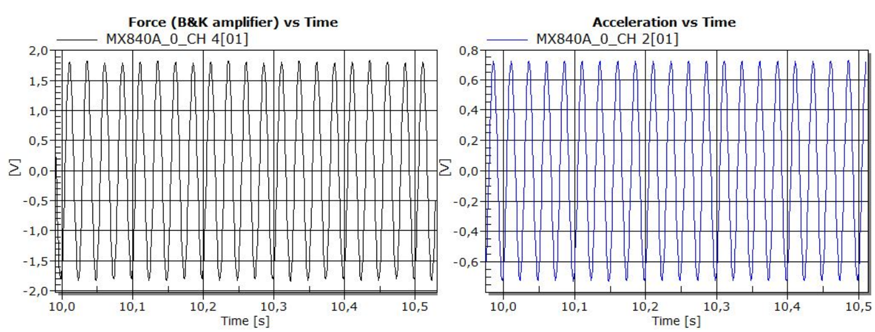

(b) Force and Acceleration Graphs (V), zoomed version

Figure 4.9: Force (B&K amplifier) and Acceleration Graphs (V)

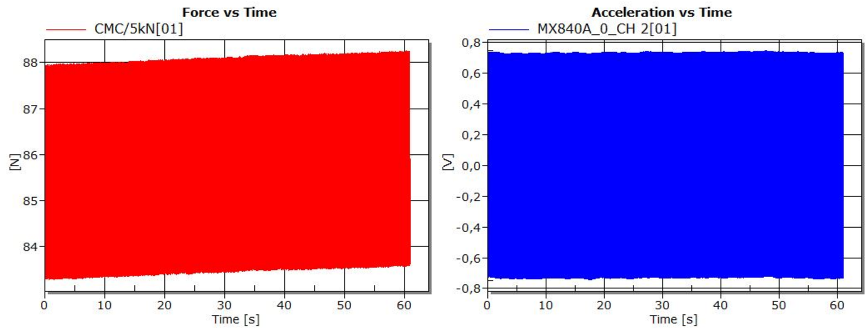

(a) Force (N) and Acceleration Graphs (V)

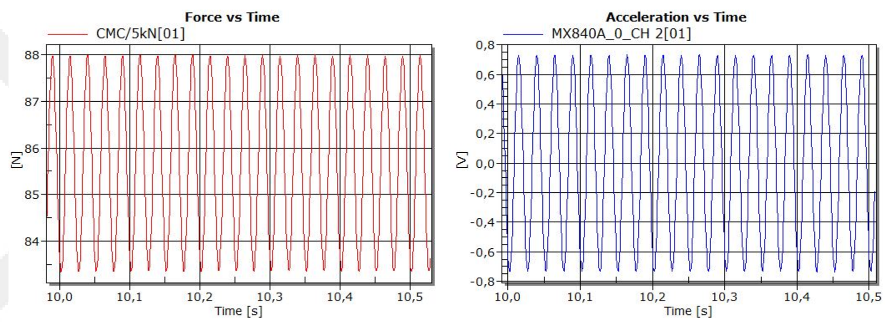

(b) Force (N) and Acceleration Graphs (V), zoomed version

Figure 4.10: Force (HBM amplifier) and Acceleration Graphs

4.3 Capacitive sensor

The capacitive sensor, PI D-510.101, is used for non-contact displacement measurements for both static and dynamic applications. The sensor face is placed parallel to the conductive surface [40]. The required gap between the sensor and the conductive surface depends on the sensor type. For instance, in the setup used here, the gap is less than 1 mm. Capacitance depends on the distance between the surfaces, so displacement change of the target surface can be measured. Capacitive sensor specifications are given in Table 4.8 [41]:

Table 4.8: Capacitive sensor D510.101 specifications

Nominal measurement range (μm)	100
max. gap (μm)	750
min. gap (μm)	50
Static resolution	< 0.001 % of measurement range
Dynamic resolution	< 0.002 % of measurement range
Sensitivity	5 μm/V

4.3.1 Capacitive sensor calibration

The capacitive sensor is calibrated in order to confirm sensitivity information given at datasheet. It is calibrated for only DC case. If experiment results and given information are not consistent, then calibration for AC case is also necessary. Experiment results are presented above confirm the sensitivity information.

For calibration, laser, multimeter, PZT actuator and motion stage, Mikrotools DT 110 EDM machine are used. Firstly, laser is a reference measuring device. Mikrotools and PZT-actuated motion stage provide the motion and thus laser and capacitive sensor are mounted to these systems. As shown in Table 4.8, static resolution of the sensor is less than 1 nm and thus 1 nm change in the motion system should be sensed by capacitive sensor. However, detecting 1 nm change depends on the instruments used and environmental conditions such as vibration, temperature or humidity.

a) Measurement with Mikrotools

Both a capacitive sensor and a retroreflector of laser are mounted on the motion stage that can be seen in Figure 4.11. The experiments are conducted for step size 500 nm, 1 μm and 5 μm. Capacitive sensor vs laser displacements graphs are obtained.

Figure 4.12-4.14 indicate the laser displacement versus capacitive sensor voltage

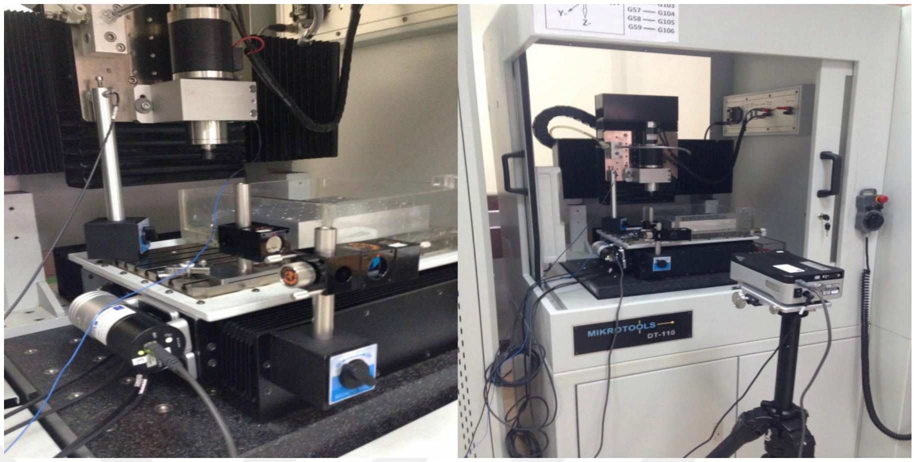

Figure 4.11: Mikrotools, calibration setup 1

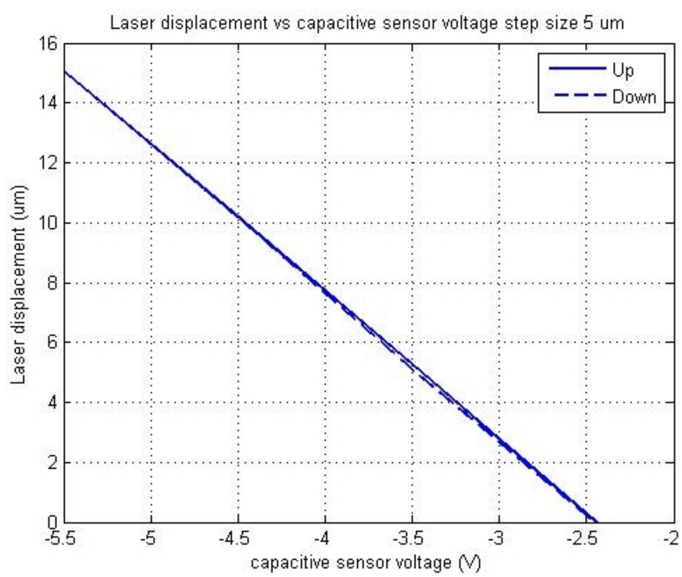

Figure 4.12: Laser displacement vs capacitive sensor voltage step size 5 um

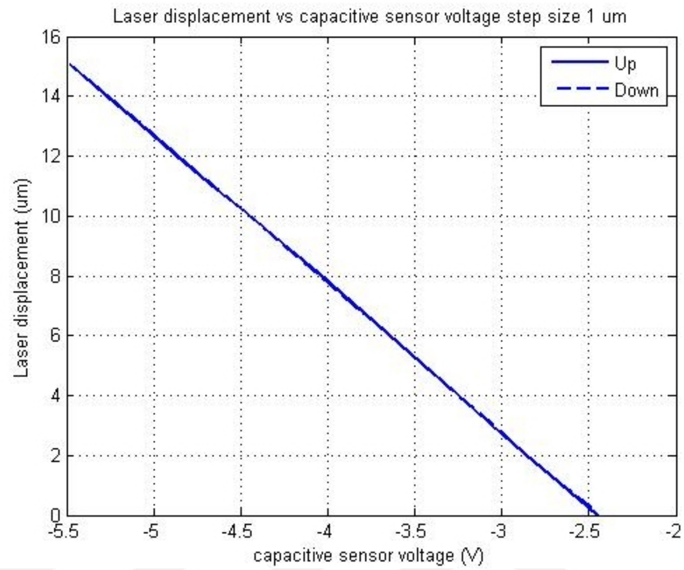

Figure 4.13: Laser displacement vs capacitive sensor voltage step size 1 um

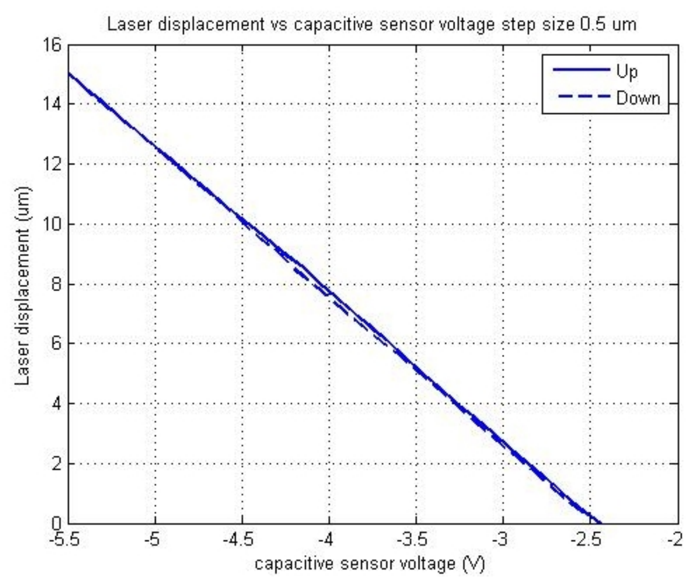

Figure 4.14: Laser displacement vs capacitive sensor voltage step size 500 nm

for step size 5 μm to 500 nm respectively. The experiments are repeated for increasing and decreasing step size, so up and down cases correspond to them. Aim of the plotting up and down graphs is to find out if there is a hysteresis caused by capacitive sensor with the assumption that there is no hysteresis induced by Mikrotools machine. A 15 μm displacement change is measured by laser and 3 V change is measured by capacitive sensor, which is consistent with sensitivity information given in the datasheet. Furthermore, capacitive sensor voltage shows its current position. When the distance between capacitive sensor and the measuring surface increases, the voltage increases. Since in these measurements step size of displacement is important, absolute value of the displacement that is measured by laser is taken into account.

Ideal step size for capacitive sensor voltage is determined according to sensitivity information given in Table 4.8. When the ideal step size of capacitive sensor voltage and the measured results are compared, the results are consistent Table 4.9 shows comparison between ideal case and measurement results.

Table 4.9: Comparison of ideal case and measurements

Ideal step size for capacitive sensor (V)	Ideal step size for laser displacement (μm)	Measured step size for laser displacement (μm)	Measured step size for capacitive sensor (V)
1	5	5.011±0.018	1.015±0.005
0.2	1	1.004±0.011	0.202±0.004
0.1	0.5	0.502±0.008	0.101±0.003

b) Measurement with PZT actuated motion platform

Following calibration with Mikrotools, hinge-based motion platform is used for obtaining motion with precise step sizes of less than 500 nm. The stage is actuated by piezoelectric actuator. The systems resolution depends on the hinge-based mechanism, material, PZT actuator and power source/controller of the piezo actuator that are discussed in piezoelectric actuator section.

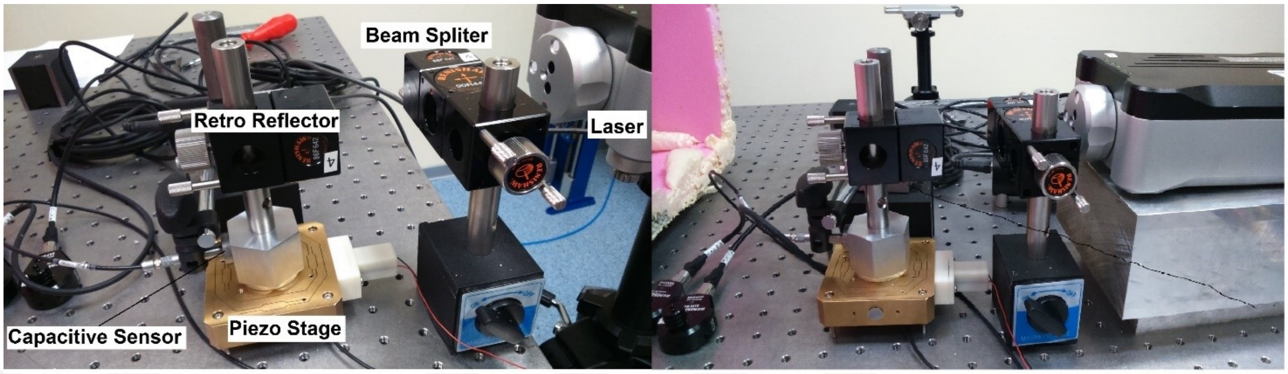

Figure 4.15: Left: first configuration is, right: the second configuration

In these measurement series, two different setup configurations are tried (see Figure 4.15). In the first configuration, laser source is on the floor, and in the second part laser source is placed on the table where the motion platform stays on. By placing the laser source on the same platform with the system, overall measurement setup is exposed to the same vibration effect. Step size 10 nm, 20 nm, 50 nm, 100 nm and 200 nm are used. Figure 4.16 -4.20 show laser displacement vs capacitive sensor voltage. 3.56 V corresponds to initial position of the capacitive sensor. In Figures 4.16 -4.20 experiment 1 shows the results belong to the first setup configuration that laser stays on the floor, and experiment 2 shows the results belong to the second setup configuration that the laser source is on the table same as the motion platform.

When experiments 1 and 2 are compared, the displacement differences for the same voltage level can be seen in the Figures 4.16 - 4.20. Especially, for experiments with step size 10 nm, the difference between two configurations is greatest among experiments because the smallest step size that is tried. Experiment 2 results approach the ideal value better than those of experiment 1. Thus, placing the laser source on same platform with the motion platform results in improvement of the measurements.

In conclusion, the capacitive sensor is calibrated with a laser as a reference instrument for displacement measurements. Two different experiment setups are used, and different step sizes are tried. Aim is to confirm the sensitivity of the capacitive sensor, and obtaining voltage vs displacement relations. The sensitivity of

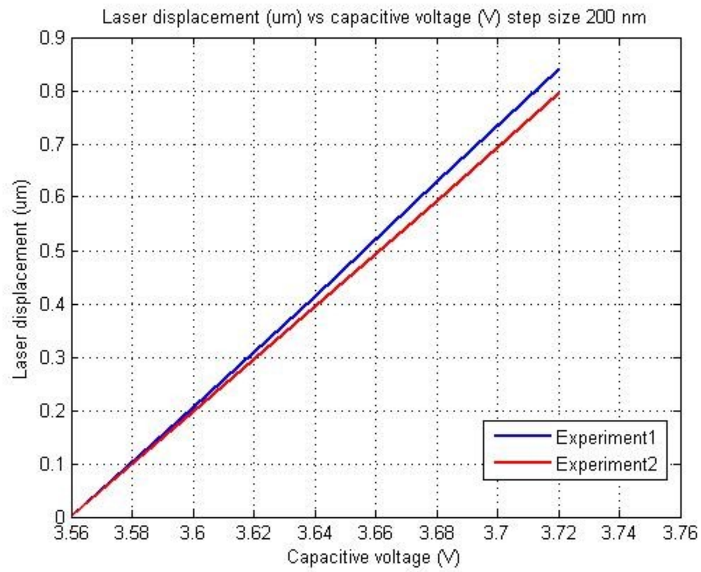

Figure 4.16: Laser displacement vs capacitive sensor voltage step size 200nm

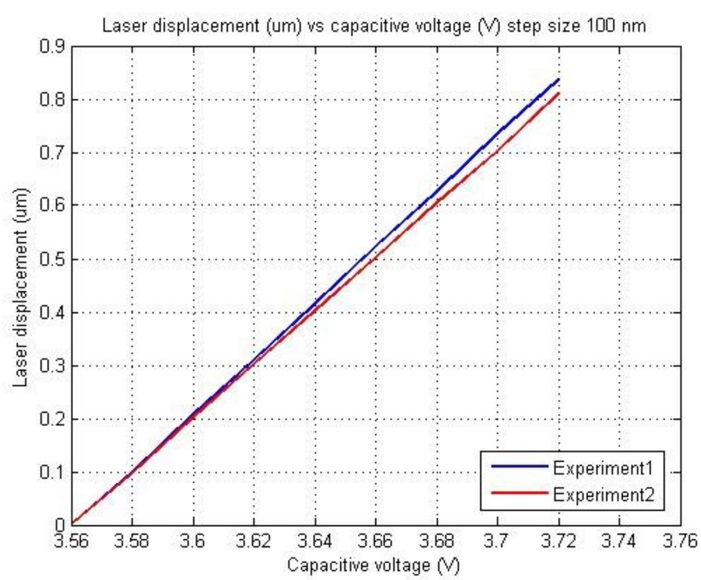

Figure 4.17: Laser displacement vs capacitive sensor voltage step size 100nm

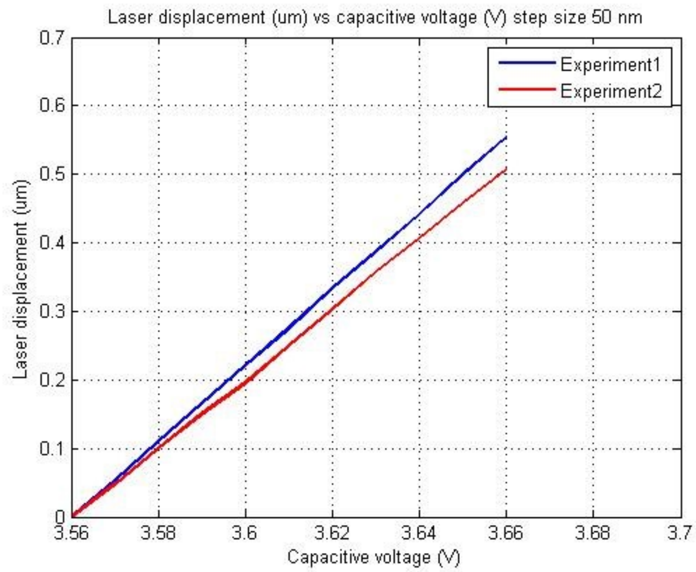

Figure 4.18: Laser displacement vs capacitive sensor voltage step size 50nm

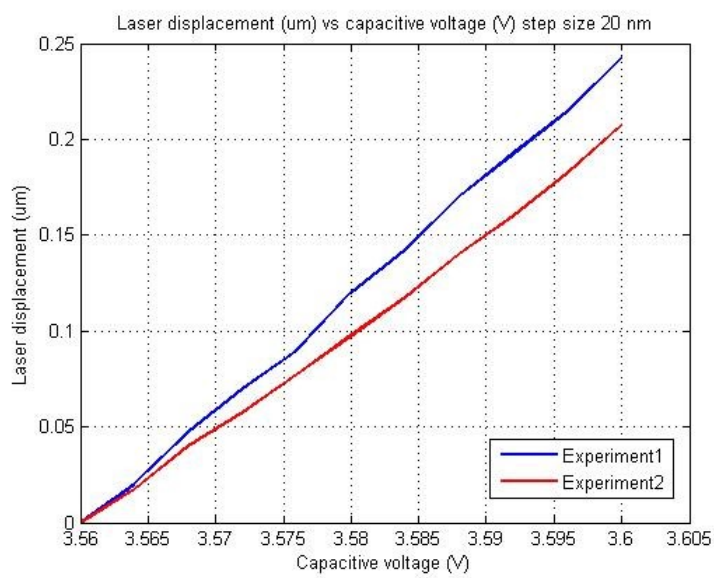

Figure 4.19: Laser displacement vs capacitive sensor voltage step size 20nm

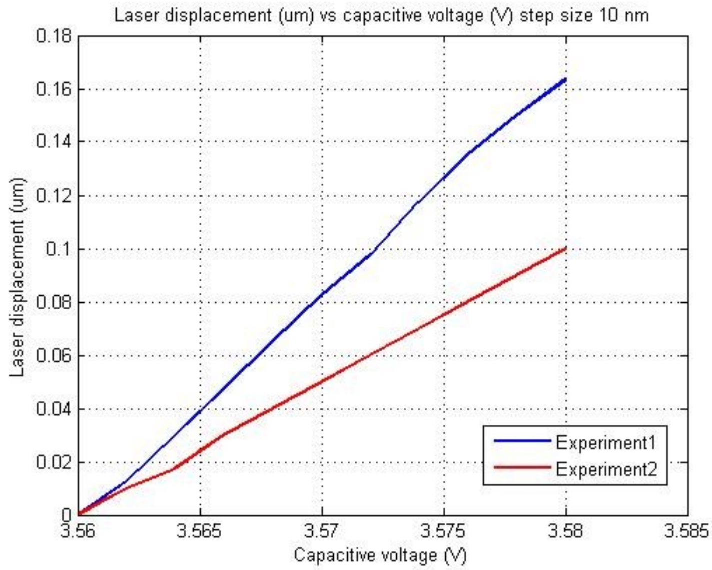

Figure 4.20: Laser displacement vs capacitive sensor voltage step size 10nm

the capacitive sensor is 5 μm/V as given in the datasheet and the measurement results are consistent. Thus, capacitive sensor can be used as a displacement sensor at DC case.

4.4 Vibrometer

Polytec OFV 5000 vibrometer controller, OFV 551/552 fiber interferometers are used to measure velocity. It is a laser-Doppler vibrometer which is based on the Doppler principle. It has two decoders; VD-09 is velocity decoder, and DD-900 is displacement decoder. These decoders have different sensitivities according to measurement range because vibrometer output range is fixed to 20 V peak-to-peak. The minimum sensitivity of VD-09 decoder is 5 mm/s/V and the minimum detectable velocity is 0.02 μm/s. The minimum sensitivity of displacement decoder DD-900 is 50 nm/V and resolution is 0.015 nm [42]. As a result, measurements with vibrometer is expected to give the most accurate results, so vibrometer is preferred to measure velocity of the motion platform in this project.

Finally, Table 4.10 show the list of instruments that are used for measurement and calibration, and Figure 4.21 indicate the test setup. When advantages and disadvantages of PZT actuator are considered, high-resolution motion is expected. However, problems such as hysteresis exist. Since the design of a controller to PZT actuator is beyond the scope of this project hysteresis and drift for DC case were not eliminated. Since drift of PZT actuator can be overcome by operating with AC, working at dynamic conditions are better suited. However, amplitude and frequency of the input should be monitored in order to prevent overheating. Furthermore, force drift is obvious, and force drift does not depend on the amplitude, frequency or DC level of the input signal. It is solved by changing the charge amplifier, so force transducer is calibrated. The sensitivity of the force transducer is 1.263 N/V, and this is used during the characterization experiments. Moreover, DC force, or preload, is not measured by force transducer with B&K amplifier because amplifier has high-pass filter and thus it only shows AC force. This feature also determines operating conditions of the device. Capacitive sensor is calibrated in order to verify the stated sensitivity. Laser and capacitive sensor resolutions are approximately same according to experiments. However, problem of using capacitive sensor is that a maximum 750 μm gap can be used to obtain accurate results. When gap is small, it affects the vibration of the stage. The details of these experiments are discussed in the next section. The displacement can also be measured by a vibrometer but main purpose of vibrometer is to measure velocity. Thus, force and velocity results of the device can be obtained by using these instruments.

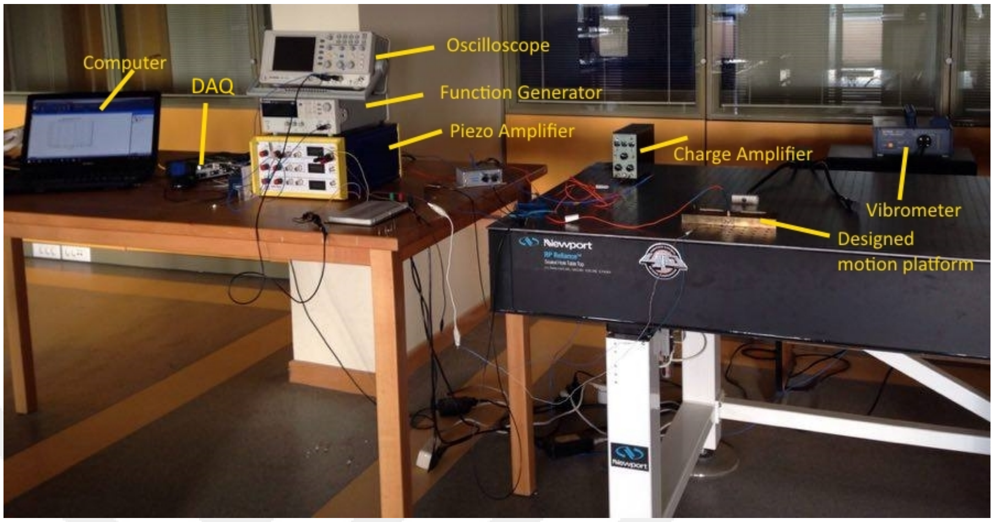

Figure 4.21: Experiment setup

Table 4.10: List of instruments

Device	Aim
Pst 150/10x10/40 Piezo actuator	Actuation
HBM CFT 5KN Force transducer	Force measurement
HBM CMA39 Charge Amplifier	Charge amplifier of force transducer
B&K Type 2635 Charge Amplifier	Charge amplifier of force transducer
OFV 5000, OFV 551/552 Vibrometer	Velocity measurement
PI D-510.101 Capacitive sensor	Displacement measurement
PISeca Signal conditioner E-82	Signal conditioner of capacitive sensor
Dytran 3035B1G accelerometer	Measure acceleration during force calibration
B&K Type 4824 Modal exciter	Actuation during force calibration
Renishaw XL 80 laser system	Measure displacement at capacitive sensor calibration
Mikrotools DT 110	Motion platform at capacitive sensor calibration
Hinge based positioning system	Motion platform at capacitive sensor calibration.
SVR 150/3/Pst Piezo amplifier	Power source and amplifier of PZT actuator
GW Instek SFG 2004 Function generator	Apply sinusoidal input to actuator
GW Instek GDS 1052U Oscilloscope	Observe input signal
Microphone G.R.A.S type 26 CA	Measurement of natural frequency

Chapter 5

System characterization

The micro mechanical test device described in this thesis is characterized to understand its behavior under different operating conditions. Force is generated by a piezo actuator, and resultant velocity is measured by a vibrometer. Measurements are made under different input voltages to the piezo actuator.

Firstly, force and velocity results are presented. The results are analyzed in terms of repeatability and linearity. Power dissipation of the system is obtained using force-velocity plots. Secondly, natural frequencies of the device are determined. Finally, limitations on the use of a capacitive sensor and displacement results are discussed.

5.1 Force and velocity measurements

A sine wave AC voltage superimposed on a DC voltage is given as an input. When DC voltage is applied to the piezo actuator, force and velocity results differ from those without DC voltage because DC voltage develops a preload effect on the system. Experiments are carried out under different mean (DC) voltages which are 0 V, 10 V, 30 V and 50 V. DC voltages are increased and decreased during a given test sequence to see its effect on the amplitudes of force and velocity.

Additionally, frequency of the input is changed in order to observe frequency effects on the system. Measurements are made at 5 Hz, 20 Hz and 40 Hz.

Nominally the same amplitudes of the AC input voltage with different mean voltages are attempted. Although piezo amplifier gain does not change during these experiments, the amplitudes of AC input slightly change with respect to DC voltage applied to piezo actuator. Furthermore, under constant DC voltage, the amplitude of sine wave changes approximately %2.5 during the experiments. Thus, there is an uncertainty related to amplitude of input. Since piezo actuator input voltage range is from -30 V to 150 V, the applied AC signal should also be in this range. Otherwise, the signal is clipped which can result in distorted output. The DC voltage levels used here provides a safe working region.

The first natural frequency of the device calculated using FEA is around 56 Hz. As a result the operating frequencies are selected to be lower than the first natural frequency in order to avoid damaging the motion platform. The maximum frequency examined is 40 Hz. Furthermore, the effect of overheating problem of PZT actuator should be considered at higher frequencies.

Initially, the system is preloaded mechanically from one side of the force transducer. However, mechanical preload cannot be determined by using force transducers are not amenable to static force measurements. To mitigate potential problems the mechanical preload is kept the same during all experiments.

One side of the platform is fixed by force transducer support part, which gives a preload to system. The other side is moving. When DC voltage is increased piezo actuator expands, and the motion stage moves in response. Thus, DC voltage effect can be considered as preload. Similar to a mechanical preload, preload caused by DC voltages is filtered by force transducer charge amplifier used here. As a result, one of the uncertainty of the system is unknown preloads.

Results below show forces and respective velocities at different frequencies and different DC voltages.

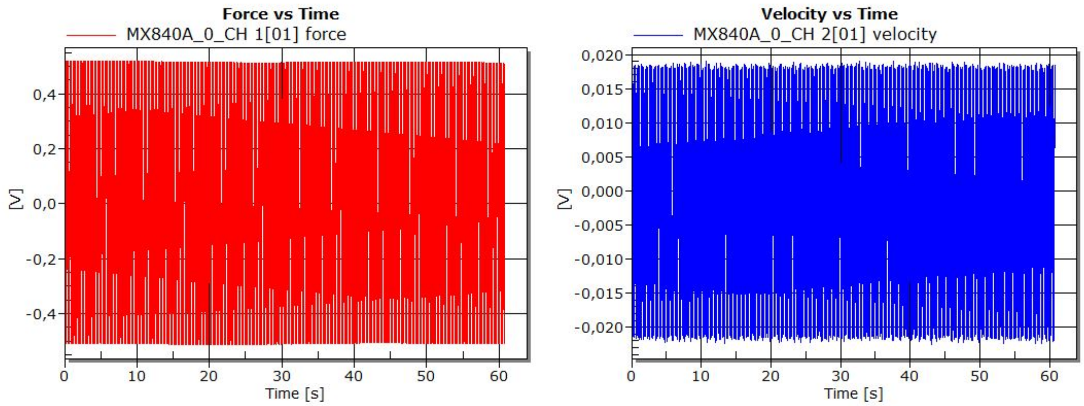

(a) Force and Velocity at 5 Hz, 60 sec.

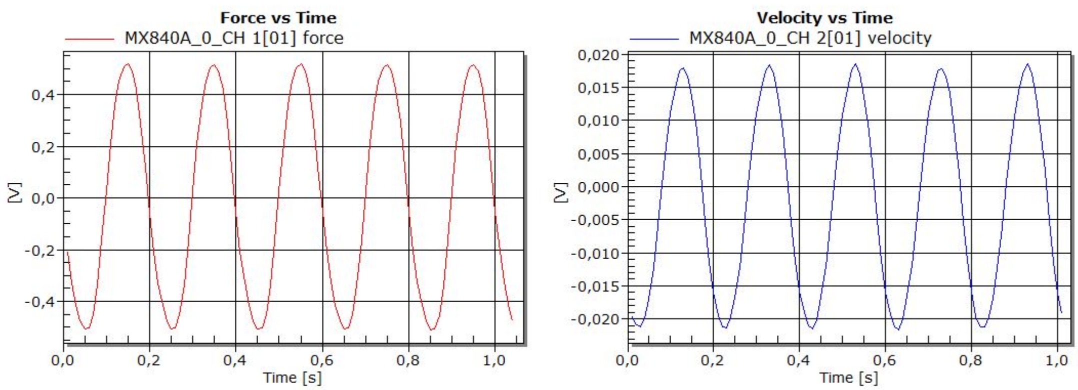

(b) Force and Velocity at 5 Hz, 1 sec.

Figure 5.1: Force and Velocity at 5 Hz

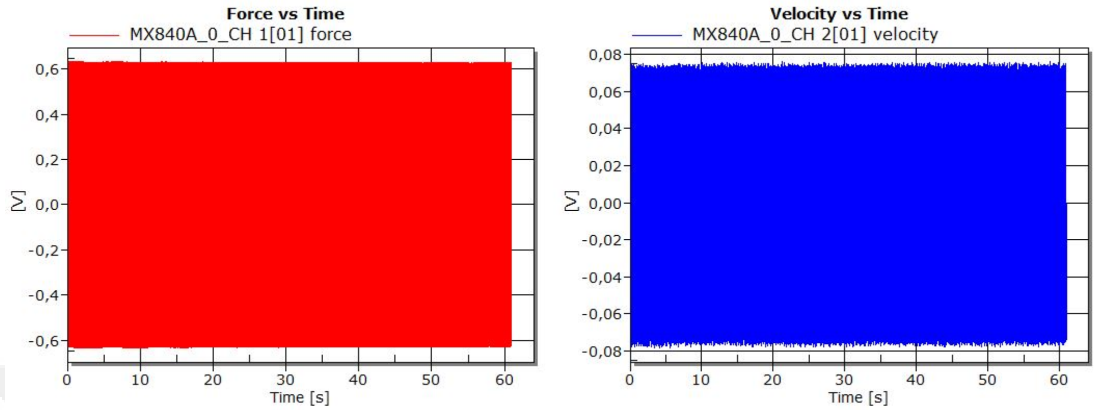

(a) Force and Velocity at 20 Hz, 60 sec.

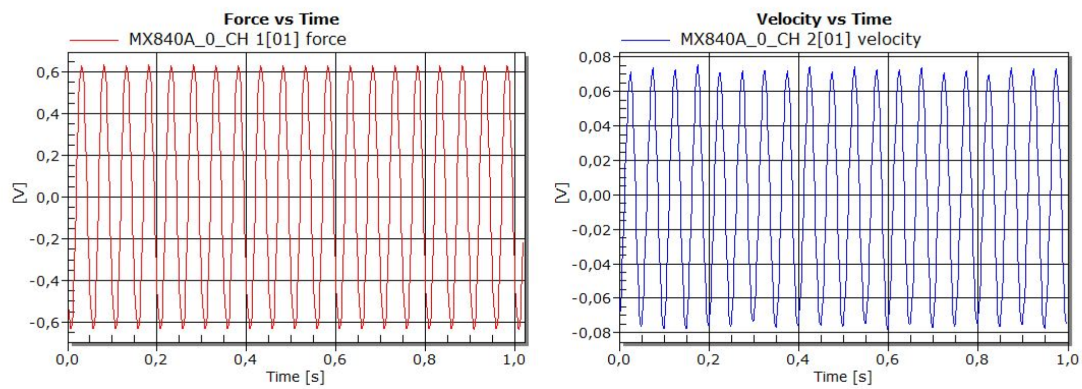

(b) Force and Velocity at 20 Hz, 1 sec.

Figure 5.2: Force and Velocity at 20 Hz

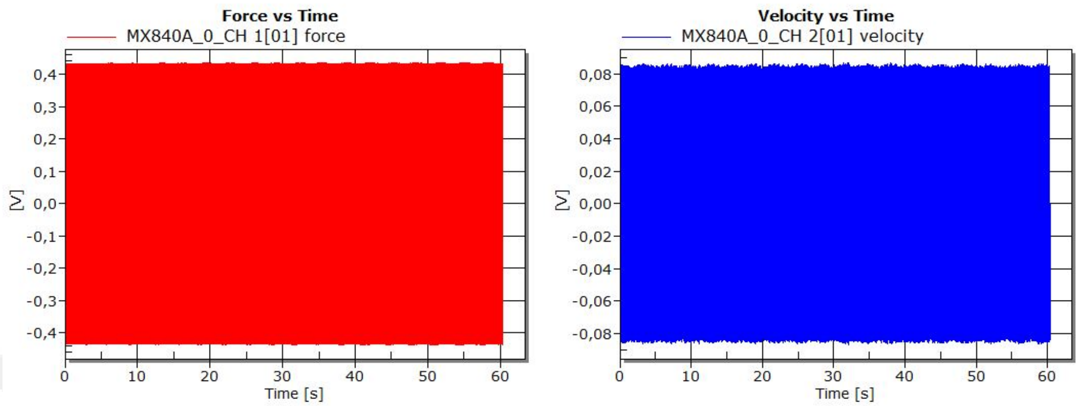

(a) Force and Velocity at 40 Hz, 60 sec.

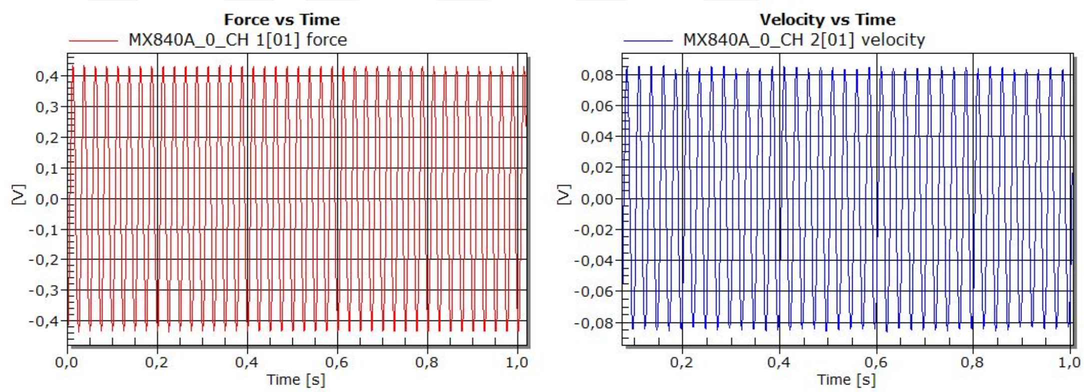

(b) Force and Velocity at 40 Hz, 1 sec.

Figure 5.3: Force and Velocity at 40 Hz

Figure 5.1-5.3 show the force and velocity results at 5, 20 and 40 Hz at 0 V DC. The minimum sensitivity of vibrometer is 5 mm/s/V, hence the corresponding range of velocity is around 100 μm/s at 5 Hz. Important point of these graphs is that upper and lower values of velocity are not equal at low frequencies, suggesting a displacement drift. This difference is obvious at 5 Hz, and reduces as frequency increases. One possible reason is that the voltage level is too low, around 20 mV at 5 Hz, so measurements can be affected easily by electrical and environmental noise. Another possible reason is that the motion stage can cause this problem. Piezo actuator pushes the motion stage forward, then the motion stage comes back by itself, without a mechanism to pull the motion stage back. So for low velocity case, the motion stage may not be able to spring back on its own with the same velocity it is pushed. Therefore, drift at low velocities, is reflected as the maximum and the minimum peak difference at velocity results. When velocity at 5 Hz is integrated with respect to time, drift is approximately 600 μm in 1 minute, which corresponds to a 2 μm drift per cycle. Since the displacement amplitude is approximately 3 μm, the motion platform itself can cause this drift. Even there is a drift caused by motion platform itself, error caused by noise should be considered. Finally, there is an input voltage threshold for obtaining equal upper and lower peaks of velocity data. It is approximately 0.08 V and corresponds to 400 μm/s. Therefore, frequency and input voltage level that produces 400 μm/s should be targeted for minimum drift conditions.

Table 5.1: 5 Hz Force vs Velocity

Input voltage (V)			Force (N) peak to peak	Velocity (μm/s) peak to peak
0 V DC	(15.7± 0.06)*sin(2πft)	up	1.138 ± 0.072	196.5 ± 1.9
	(15.7± 0.06)*sin(2πft)	down	1.137 ± 0.060	202.7 ± 0.7
10 V DC	(15.95± 0.06)*sin(2πft)	up	1.096 ± 0.072	204.5 ± 1.5
	(15,95± 0.06)*sin(2πft)	down	1.090 ± 0.057	213.1 ± 0.8
30 V DC	(16.30± 0.06)*sin(2πft)	up	0.976 ± 0.056	220.6 ± 0.9
	(16.35± 0.06)*sin(2πft)	down	0.963 ± 0.045	224.6 ± 1.1
50 V DC	(16.7 ± 0.1)*sin(2πft)	up	0.951 ± 0.065	221.9 ± 0.6

Table 5.2: 20 Hz Force vs Velocity

Input voltage (V)			Force (N) peak to peak	Velocity (μm/s) peak to peak
0 V DC	(15.2 ± 0.07)*sin(2πft)	up	1.467 ± 0.054	738.8 ± 4.9
	(14.9 ± 0.19)*sin2πft)	down	1.447 ± 0.031	729.6 ± 9.6
10 V DC	(15.5 ± 0.05)*sin(2πft)	up	1.420 ± 0.053	776.7 ± 5.4
	(15.4 ± 0.16)*sin(2πft)	down	1.387 ± 0.047	783.9 ± 7.5
30 V DC	(16.5 ± 0.09)*sin(2πft)	up	1.295 ± 0.06	871.2 ± 7.7
	(16.55 ± 0.13)*sin(2πft)	down	1.268 ± 0.045	883.5 ± 8
50 V DC	(17.75 ± 0.09)*sin(2πft)	up	1.296 ± 0.078	931.8 ± 7.5

Table 5.3: 40 Hz Force vs Velocity

Input voltage			Force (N) peak to peak	Velocity (μm/s) peak to peak
10 V DC	(11)*sin(2πft)	up	(1.247 ± 0.042)	(998.7 ± 29)
	(11.1 ± 0.33)*sin(2πft)	down	(1.240 ± 0.036)	(1058.1 ± 71.9)
30 V DC	(12 ± 0.29)*sin(2πft)	up	(1.137 ± 0.038)	(1149.9 ± 34.1)
	(11.9 ± 0.37)*sin(2πft)	down	(1.112 ± 0.026)	(1132.2 ± 24.3)
50 V DC	(13.05 ± 0.29)*sin(2πft)	up	(1.100 ± 0.061)	(1264.9 ± 35.1)

Table 5.1- 5.3 show force and velocity results with respect to input voltage. Up refers to DC voltage being increased from 0 V to 50 V, and down refers to voltage being decreased from 50 to 0 V. One minute of data are saved for each experiment, then peak-to-peak values of force and velocity are calculated using MatLab. MatLab codes are in given Appendix B. The data shown in Tables 5.1-5.3 are peak-to-peak values because of differences between upper and lower peaks of velocity.

When the input is same for up and down cases, force and velocity values are close each other. Up cases of force and velocity differ less than %10 from down cases. The difference depends on both input change and hysteresis behavior of piezo actuator.

Behavior of force and velocity with respect to DC voltage is a significant in characterizing the system because increase in DC voltage leads to decrease in force and increase in velocity. The results of force and velocity measurement applying nomially same AC voltage but with different DC values are shown in Table 5.1-5.3.

These results can be interpreted considering two physical behaviors. The first one is the boundary condition of the piezo actuator. When piezo actuator is combined with a spring mechanisms, in this case the motion platform is considered as spring, the stroke and the generated force of actuator is reduced from their maximum values. When the stiffness of the spring mechanism is low, PZT actuator can move easily and does not generate higher forces.

The second one is the stiffness of the piezo actuator under DC voltages. Applying DC voltage to the piezo actuator stretches the actuator resulting in reduction of generating force with same input. PZT actuator becomes more stiff when applied DC voltage increased. Thus, generated force decreases and velocity increases. As a result, applying DC voltage (preload) changes the velocity and force values in dynamic case.

Additionally, the velocity increases with the frequency as expected because it is proportional to angular frequency. For 40 Hz case, the amplitude of input is reduced to around 10 V because higher than 10 V value of amplitude, especially for 0 V DC case, causes distortion at the output. However, when the input amplitude decreases, the velocity also decreases but very low velocity is not preferred due to observing difference between upper and lower peaks at velocity results. Thus, 15 V and higher voltages is acceptable for low frequencies whereas for higher frequencies lower input voltage is required due to absence of distortions. To approach the 15 V at 40 Hz, higher than 10 V input is applied but for 0 V DC case it is not feasible, so the results are not included in the Table 5.3. For instance, 0 V DC, 9.6 $\sin(2\pi 40t)$ input is given and, 1.095 N peak-to-peak and 841 μm/s peak-to-peak is obtained.

Power dissipation graphs presented in Figures 5.4-5.6. The up cases are shown. The area of the graphs represent power dissipation. Power dissipation increases with the operated frequency increases. For 40 Hz case, even the input is less than 5 Hz case, power dissipation is greater than 5 Hz case. Furthermore, DC voltage effect can be seen from power dissipation graphs as increase in DC voltage results in increasing velocity and decreasing force. Thus, each mean voltage graph is not overlapping as expected.

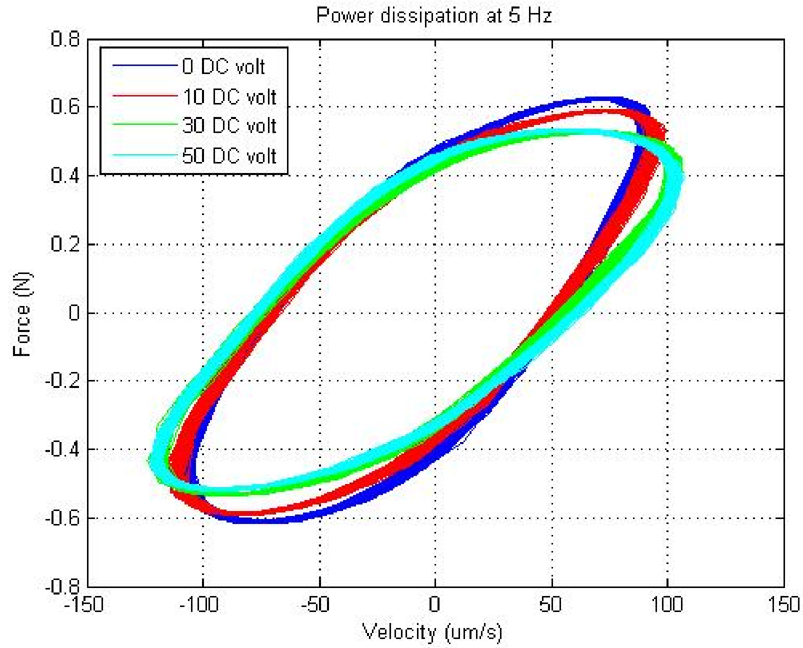

Figure 5.4: Power dissipation at 5 Hz

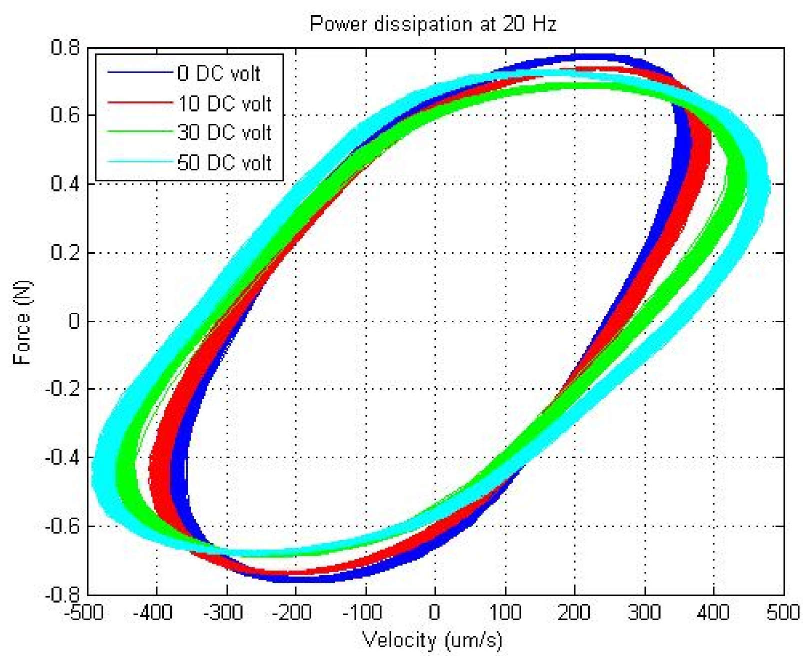

Figure 5.5: Power dissipation at 20 Hz

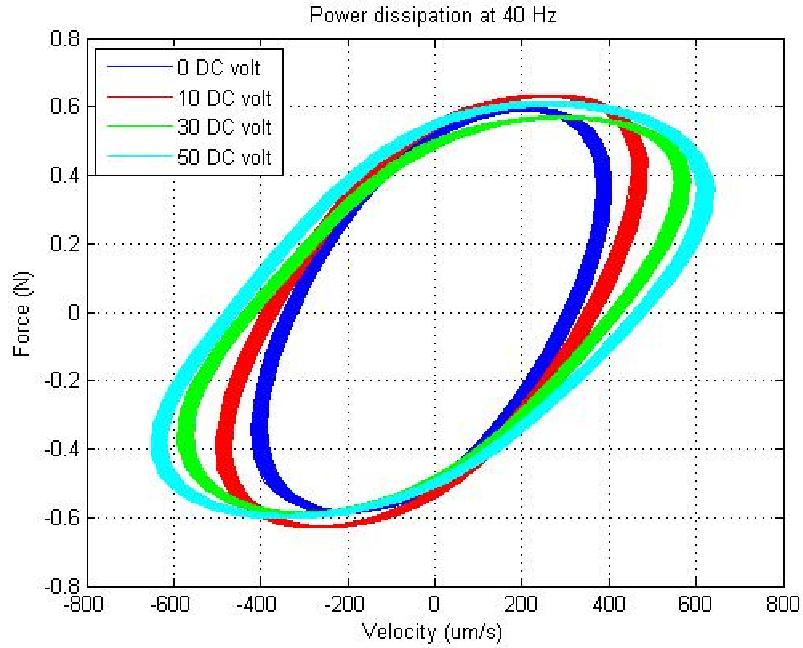

Figure 5.6: Power dissipation at 40 Hz

5.2 Linearity

Experiments are conducted in order to determine the linearity of the device. The tests are performed at different frequencies such as 5 and 20 Hz and different DC voltages such as 0 V and 10 V. When input amplitude is doubled at 5 Hz with a mean 0 V force increased 1.657 $\pm$ 0.006 times whereas velocity increased 2.14 $\pm$ 0.036 times. Then the same test is repeated at 5 Hz with a mean 10 V to understand the DC voltage effect on the linearity. Force increased 1.63$\pm$ 0.006 times and velocity increased to 2.23$\pm$ 0.023 times. Based on these results, DC voltage does not have an effect on linearity for 5 Hz. When input amplitude is doubled at 20 Hz, 0 V, force increased 1.72$\pm$ 0.01 times and velocity increases 2.23$\pm$ 0.058 times. Similar to 5 Hz experiments, 10 V DC voltage is applied at 20 Hz cases. In this case, force increased 1.65$\pm$ 0.009 times and velocity increased 2.19 $\pm$ 0.04 times.

These measurements show that under different frequencies and DC input values force and velocity response are approximately constant and directly proportional to input AC voltage but not linearly. The measured velocity and force response show a nearly constant impedance.

5.3 Repeatability and Uncertainty

Force and velocity tests are performed under the same conditions, in a short time period to determine whether results are repeatable or not. Experiments are carried out at both successive days and different times of the same day. However, determining repeatability of the results are not easy because of uncontrolled variations at input. 40 Hz, 10 V DC up case is analyzed because there is no input AC voltage variations for all tests. Force results differ from each other by % 7.6 and velocity results vary from each other by % 5.8. Results are repeatable with less than %10 error.

The uncertainties affect repeatability and they are due to hysteresis properties of piezo actuator, nonlinearity of motion platform, accelerometer used in calibrating force transducer, which has a sensitivity 1 mV/m/s^2 ± %10, uncontrolled environmental conditions, the mechanical preload.

Uncertainty of velocity data is high when compared to force data according to Tables 5.1- 5.3. Furthermore, 5 and 20 Hz velocity results vary less when compared to 40 Hz data. As a result, working at low frequency is preferable.

5.4 Capacitive displacement sensor results

When using a capacitive sensor to measure displacement of a vibrating surface in close proximity, the thin air space acts like a spring and damper, such a behavior can influence the motion of the surface, in this case primary stage surface. Displacement measurements made using a capacitive sensor are compared with those by a vibrometer. The vibrometer can be used to measure displacement, but it shows drift until it reaches its maximum voltage. Since source of drift is important for device characterization, vibrometer is used for only velocity measurements. Capacitive sensor results are compared in order to understand whether capacitive sensor can be used or not. The experiments are conducted under different DC voltages at an operating frequency is 5 Hz. Up and down cases are examined similar to force-velocity measurement experiments. Note that the mechanical preload is different than the results are shown above.

Table 5.4: Force and Vibrometer Displacement

Input voltage (V)			Force (N) peak to peak	Displacement (μm) peak to peak
0 V DC	(16.2)*sin(2πft)	up	2.103 ± 0.003	5.972 ± 0.002
	(16.0)*sin(2πft)	down	1.944 ± 0.011	6.192 ± 0.019
10 V DC	(16.3 ± 0.1)*sin(2πft)	up	1.970 ± 0.012	6.202 ± 0.10
	(16.2)*sin(2πft)	down	1.850 ± 0.018	6.507 ± 0.016
30 V DC	(16.7 ± 0.1)*sin(2πft)	up	1.699 ± 0.004	6.577 ± 0.017
	(16.6)*sin(2πft)	down	1.630 ± 0.021	6.729 ± 0.012
50 V DC	(17.2 ± 0.1)*sin(2πft)	up	1.279 ± 0.007	6.686 ± 0.021

Table 5.5: Force and Capacitive Sensor Displacement

Input voltage (V)			Force (N) peak to peak	Displacement (μm) peak to peak
0 V DC	(16.3 ± 0.1)*sin(2πft)	up	0.876 ± 0.026	6.775 ± 0.009
	(16.1 ± 0.1)*sin(2πft)	down	1.912 ± 0.121	6.612 ± 0.083
10 V DC	(16.4)*sin(2πft)	up	0.838 ± 0.083	6.876 ± 0.070
	(16.2)*sin(2πft)	down	1.076 ± 0.112	6.876 ± 0.085
30 V DC	(16.6)*sin(2πft)	up	0.742 ± 0.122	7.034 ± 0.096
	(16.8)*sin(2πft)	down	0.804 ± 0.092	7.100 ± 0.081
50 V DC	(17.2)*sin(2πft)	up	0.600 ± 0.085	6.988 ± 0.070

A characteristic the device described here is that force decreases with increase in DC voltage in contrast to displacement behavior, so results in Table 5.5 are expected. As shown in Table 5.4 and 5.5, capacitive sensor results are different than vibrometer results. This difference is especially obvious in the force results.

When a vibrating plate is placed very close to a rigid planar surface, vibrational damping rate is increased. Fluid layer between the plates has a damping contribution, and the thickness of fluid layer, and operating frequency are significant parameters for determining damping that is caused by fluid layer [43]. In the experiment setup used here, primary stage vibrates and the capacitive sensor acts as a rigid plate, so air between the plates produces a damping effect. The capacitive sensor is close to the motion stage, less than 1 mm, leading to damping. Thus, force value decreases when capacitive sensor used. 50 V DC case shows the lowest force value because PZT actuator expands and approaches the capacitive sensor, so gap becomes smaller. Therefore, measurements with capacitive sensor show different force and velocity results than vibrometer results because of damping, and for dynamic case capacitive sensor is not preferred for displacement measurements.

However, an interesting outcome of capacitive sensor displacement measurement is that capacitive sensor does not show displacement drift, shown in Figure 5.7. Capacitive sensor voltage oscillates around 8.8 V which corresponds to the position of capacitive sensor. The sensitivity of the sensor is 5 μm/s. If the system has a drift, it is expected that capacitive sensor could sense the drift because drift at DC case is measurable by capacitive sensor. Figure 5.8 shows drift measured by this sensor.

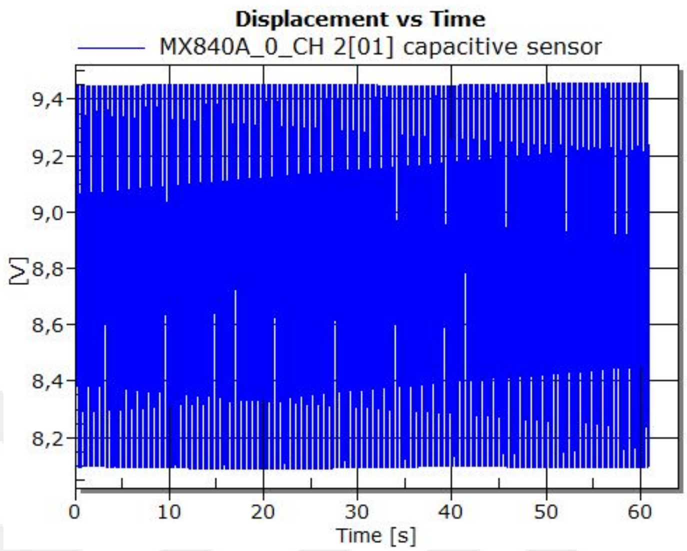

Figure 5.7: Displacement measurement by capacitive sensor at 5 Hz

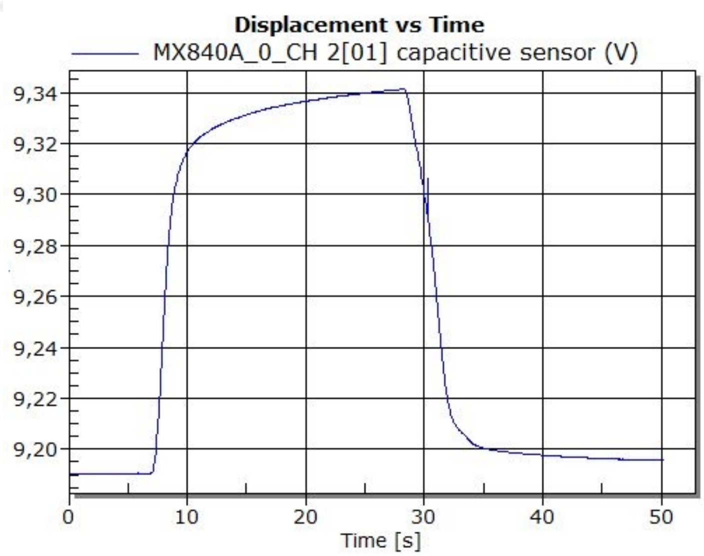

Figure 5.8: Displacement measurement by capacitive sensor at DC case

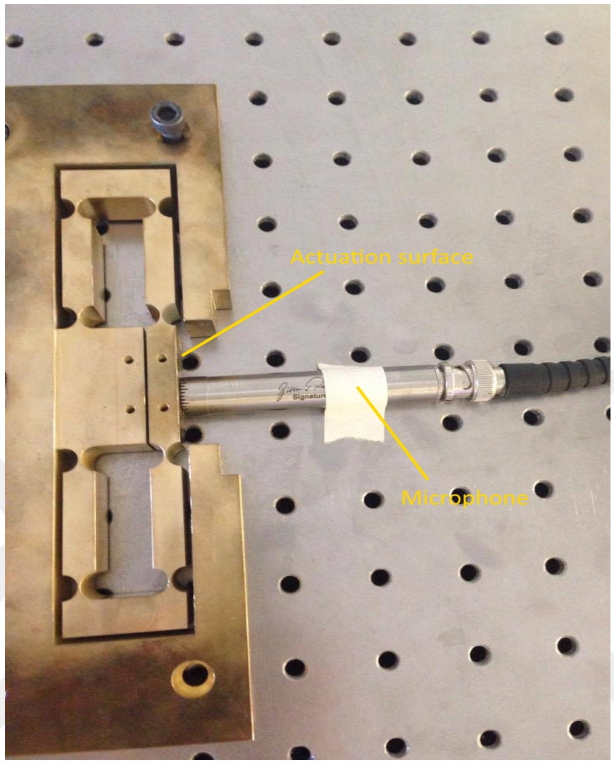

Figure 5.9: Natural Frequency measurements setup

5.5 Natural Frequency Measurements

Natural frequencies of the motion stage are necessary to determine the operating frequency limits of a device. Impulse force is given to the primary stage and frequency spectrum of output response is measured. In order to not load the primary stage surface with an accelerometer a microphone is placed in close proximity to determine the natural frequencies.

Experimental setup is shown in Figure 5.9. An impulse is given by a small hammer and applied to outer surface of primary stage. First four natural frequencies are measured, shown in Figure 5.10 and they are 56.25 Hz, 68.75 Hz, 159.375 and 190.625 Hz. Measured frequencies are not sharp peaks because of damping of the device described here.

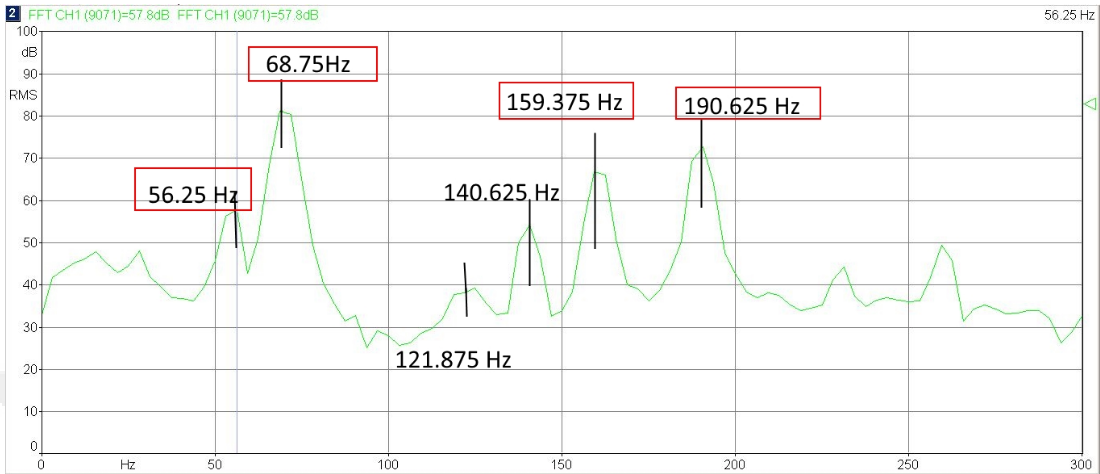

Figure 5.10: Measured natural frequencies

Response of 56.25 Hz is small compared to 68.75 Hz because FEA proves that first mode shape is not along the actuation direction and 68.75 Hz is dominant natural frequency. Furthermore, 121.8 and 140.6 are measured as they are the harmonics of 56.25 and 68.75 Hz.

The measured natural frequencies are very close to those obtained by FEA. The measured first natural frequency is approximately same with the first calculated natural frequency by FEA. The measured second and fourth natural frequencies differ by % 6 from those obtained by FEA. The third measured natural frequency differs by % 14 from the calculated third natural frequency by FEA.

In the present case, the important natural frequency is the first one because it determines the upper limit of the operating frequency of the device. Therefore, operating frequencies which are higher than 40 Hz is not suggested due to approaching the natural frequency.

In summary, the device is characterized in terms of force velocity relation, linearity and repeatability. Both AC and DC voltage are applied to the actuator, resultant force and velocity are measured. While AC voltage is approximately the same for each experiment, different DC voltage levels are applied to the actuator. As characteristics of device, increase in DC voltage leads to increase in velocity in contrast to force. Increasing and decreasing DC voltage produce different force and velocity results at the same voltage, but the difference is less than %10. The device can operate up to 40 Hz at high input AC voltages. However, if device operates at higher than 40 Hz, input should be limited up to 20 V peak-to-peak due to output distortion. Furthermore, slight frequency changes are observed at higher frequencies in velocity output, which makes the device less reliable at high frequencies. On the other hand, at 40 Hz velocity magnitude increases, and the maximum and minimum peak values become equal. Thus, displacement drift is eliminated. Unknown mechanical preload, uncontrolled environmental conditions, hysteresis property of piezo actuator, uncontrolled input is given to actuator cause uncertainties in the system. All these uncertanties affect repeatability but results are repeatable with less than %10 error. Additionally, force and velocity responses are directly proportional to input AC voltage but not linearly. Lastly, natural frequencies are measured, and first two natural frequencies are 56.25 Hz and 68.75 Hz. These are important to define operating frequency range of the device. Thus, lower operating frequencies are suggested due to low natural frequencies of the device.

Chapter 6

Conclusion

6.1 Conclusion

Work presented in this thesis describes design and characterization of a micro mechanical test device. Starting point of this thesis is design of a micro tensile test device for static tests which is then extended to operate dynamically. The device includes subsystems for actuation, measurement of stress and strain, sample gripper, and specimen preparation.

The motion platform of the device has a monolithic structure, which is based on circular hinges. This structure allows precise and smooth motion due to lack of joints. A prismatic mechanism based on double parallelogram is modified for use as micro mechanical test device and manufactured by electric discharge machine and milling.

The prototypes are analyzed by finite element method. An important requirement of a tensile device is to generate motion only in one direction to avoid misalignments and possible inaccuracies. It is shown that the motion stage displaces only in one direction under both static and time-dependent cases. Two different prototypes of design are analyzed. In both static and time-dependent cases, change in geometry has a negligible effect on the results. However, change of material property and boundary conditions can alter the results. For instance, under 1 N force, the motion platform moves 33.9 μm. In reality, it moves less than FEA results because material properties may differ from the actual values.

Natural frequencies of device are obtained by FEA. Since the device is designed to also operated under dynamic loads, the final version of design is simulated using FEA and results are compared with experimental results. According to analysis and experiment results, natural frequencies are approximately the same with each other, and thus FEA results are verified by measurements.

A piezo actuator,a vibrometer, a force transducer are used for actuation, velocity measurement and force measurement, respectively. Although piezo actuator can work under DC and AC conditions, vibrometer and force transducer work under AC conditions. Experiments are conducted under different input voltages. The main problem during measurements is exsitence of continuous drift in force transducer. Charge amplifier for force transducer is changed, and thus drift of force was eliminated using a charge amplifier with a high pass filter.

The device is characterized in terms of force velocity relation, linearity, repeatability, and finding natural frequencies. Operating range of the device is between 5-40 Hz, and above 800 μm/s peak-to-peak velocity. Input voltage is adjusted in order to provide velocity requirement of the device. Thus, power dissipation of sample materials can be found by comparing power dissipation of the device with and without sample.

6.2 Future Work

Future work should include improvements to the micro mechanical test device and elimination of uncertainty sources. Since aim of the test device is to determine mechanical properties such as Young's modulus, stiffness or damping of micro-scale sample, displacement versus force graphs should be obtained. Displacement should be measured by a reliable sensor.

Furthermore, if piezo actuator is controlled by a closed loop, drift and hysteresis problem of the piezo actuator would disappear. Thus, device can operate at both DC and AC case without hysteresis and drift problems. Since input becomes controlled, variation at the input will be eliminated, so uncertainty related to input voltage will be removed.

Accurate measurements of preload will lead to more reliable tests. Finally, test conditions should be improved in order to eliminate temperature variations and environmental vibrations.

Bibliography

[1] D. Gianola and C. Eberl, "Micro- and nanoscale tensile testing of materials," *The Journal of The Minerals, Metals & Materials Society*, vol. 61, no. 3, pp. 24 – 35, 2009.

[2] K. Hemker and J. W.N. Sharpe, "Microscale characterization of mechanical properties," *Annual Review of Materials Research*, vol. 37, pp. 93 – 126, 2007.

[3] M.A.Haque and M. Saif, "In-situ tensile testing of nano-scale specimens in SEM and TEM," *Experimental Mechanics*, vol. 42, no. 1, pp. 123–128, 2002.

[4] Q. Bai, B. He, Y. Liang, and K. Cheng, "Micro-tensile device and test for micro-wire in mems," in *Automation and Computing (ICAC), 2012 18th International Conference on*, pp. 1–4, 2012.

[5] Y.Zhu and H. D. Espinosa, "An electromechanical material testing system for in situ electron microscopy and applications," *Proceedings of the National Academy of Sciences of the United States of America (PNAS)*, vol. 102, no. 41, pp. 14503–14508, 2005.

[6] T.Hua, H.Xie, B.Pan, X.Qing, F.Dai, and X.Feng, "A new micro-tensile system for measuring the mechanical properties of low-dimensional materialsfibers and lms," *Polymer Testing*, vol. 26, pp. 513–518, 2007.

[7] S. J.Ding, Y. Meng, "Experimental and theoretical study of young modulus in micromachined polysilicon films," *Tsinghua Science and Technology*, vol. 7, no. 3, pp. 270–275, 2002.

[8] C. Seguineau, M. Ignat, C. Malhaire, S. Brida, X. Lafontan, J. Desmarres, C. Josserond, and L. Debove, “Micro-tensile tests on micromachined metal on polymer specimens: elasticity, plasticity and rupture,” *CoRR*, 2008.

[9] R. Modlinski, R. Puers, and I. D. Wolf, “AlCuMgMn micro-tensile samples: Mechanical characterization of {MEMS} materials at micro-scale,” *Sensors and Actuators A: Physical*, vol. 143, no. 1, pp. 120 –128, 2008.

[10] I. Chasiotis and W. G. Knauss, “Microtensile tests with the aid of probe microscopy for the study of mems materials,” in *Proceedings of the SPIE*, vol. 4175, pp. 92–99, 2000.

[11] J. W. N. Sharpe, B. Yuan, and R. L. Edwards, “A new technique for measuring the mechanical properties of thin films,” *Journal Of Microelectromechanical Systems*, vol. 6, no. 3, pp. 193 – 199, 1997.

[12] J. Han, M. D. Uchic, and T. Saif, “Novel MEMS apparatus for in situ thermomechanical tensile testing of materials at the micro- and nano-scale,” in *Micro Electro Mechanical Systems, 2009. MEMS 2009. IEEE 22nd International Conference on*, pp. 80–83, 2009.

[13] B. C. Prorok, Y. Zhu, H. D. Espinosa, Z. Guo, Z. P. Bazant, Y. Zhao, and B. I. Yakobson, “Micro- and nanomechanics,” *Encyclopedia of Nanoscience and Nanotechnology*, vol. 5, pp. 555–600, 2004.

[14] W. N. Sharpe, J. Pulskamp, D. S. Gianola, C. Eberl, R. G. Polcawich, and R. J. Thompson, “Strain measurements of silicon dioxide microspecimens by digital imaging processing,” *Experimental Mechanics*, vol. 47, no. 5, pp. 649–658, 2007.

[15] S. Gudlavalleti, B. P. Gearing, and L. Anand, “Flexure-based micromechanical testing machines,” *Experimental Mechanics*, vol. 45, no. 5, pp. 412–419, 2005.

[16] Y. Chao and D. Liu, “Gold wire and solder joint microforce testing using microforce tester,” *Experimental Techniques*, vol. 27, no. 5, pp. 37–40, 2003.

[17] E. Tan, S. Ng, and C. Lim, "Tensile testing of a single ultrafine polymeric fiber," *Biomaterials*, vol. 26, no. 13, pp. 1453–1456, 2005.

[18] B. Mortimer, D. R. Drodge, K. I. Dragnevski, C. R. Siviour, and C. Holland, "In situ tensile tests of single silk fibres in an environmental scanning electron microscope (esem)," *Journal of Materials Science*, vol. 48, no. 14, pp. 5055–5062, 2013.

[19] C. Szczepanski, S. Jha, P. Shade, R. Wheeler, and J. Larsen, "Demonstration of an in situ microscale fatigue testing technique on a titanium alloy," *International Journal of Fatigue*, vol. 57, pp. 131 – 139, 2013. Fatigue and Microstructure: A special issue on recent advances.

[20] H. S. Cho, K. J. Hemker, K. Lian, and J. Goettert, "Tensile, creep and fatigue properties of liga nickel structures," in *Micro Electro Mechanical Systems, 2002. The Fifteenth IEEE International Conference on*, pp. 439–442, 2002.

[21] N. Lobontiu, *Compliant Mechanisms: Design of Flexure Hinges*. Florida,USA: CRC Press, 2002.

[22] B. P. Trease, Y.-M. Moon, and S. Kota, "Design of large-displacement compliant joints," *Transactions of the ASME*, vol. 127, pp. 788–798, 2005.

[23] X. Tang and I. m. Chen, "A large-displacement 3-dof flexure parallel mechanism with decoupled kinematics structure," in *2006 IEEE/RSJ International Conference on Intelligent Robots and Systems*, pp. 1668–1673, 2006.

[24] W. Ai and Q. Xu, "New structural design of a compliant gripper based on the scott-russell mechanism," *International Journal of Advanced Robotic Systems*, pp. 1–10, 2014.

[25] Z. Wu and Y. Li, "Design, modeling, and analysis of a novel microgripper based on flexure hinges," *Advances in Mechanical Engineering*, pp. 1–11, 2014.

[26] M. Acer and A. Sabanovic, "Micro position control of a designed 3-prr compliant mechanism using experimental models," in *Control Conference (ASCC), 2013 9th Asian*, pp. 1–6, 2013.

[27] F. P. Beer, J. E. Russell Johnston, J. T. Dewolf, and D. F. Mazurek, *Mechanics of Materials*. Avenue of the Americas, New York: McGraw-Hill, 2012.

[28] Comsol, *Comsol Multiphysics Reference Manual*, 5 2013.

[29] "Meshing your geometry: When to use the various element types." https://www.comsol.com/blogs/meshingyourgeometryvariouselementtypes/. Accessed: 2015-04-10.

[30] "Size parameters for free tetrahedral meshing in comsol multiphysics." https://www.comsol.com/blogs/size_parameters_free_tetrahedral_meshing_comsolmultiphysics/. Accessed: 2015-04-18.

[31] "Theory and applications of piezo actuators and pzt nanopositioning systems." http://www.physikinstrumente.com/tutorial/. Accessed: 2016-06-15.

[32] "Piezo-mechanics: An introduction." https://www.americanpiezo.com/images/stories/content_images/pdf/apc_stack_principles.pdf. Accessed: 2015-09-28.

[33] "First steps towards piezoaction." https://www.americanpiezo.com/images/stories/content_images/pdf/httpwww.americanpiezo.comproducts_servicesstack_actuatorsapci_piezo_e_intro.pdf. Accessed: 2015-09-29.

[34] H. Jung and D.-G. Gweon, "Creep characteristics of piezoelectric actuators," *Review of Scientific Instruments*, vol. 71, no. 4, 2000.

[35] "Low voltage co-fired multilayer stacks, rings and chips for actuation." https://www.americanpiezo.com/images/stories/content_images/pdf/apc_multilayer_catalog.pdf. Accessed: 2015-09-16.

[36] "Paceline cft calibrated piezo force sensor." https://www.hbm.com/en/2917/paceline-cft-calibrated-piezo-force-transducer/. Accessed: 2015-10-25.

[37] "Pcb piezotronics: Introduction to piezoelectric force sensors." https://www.pcb.com/techsupport/tech_force.aspx. Accessed: 2016-04-25.

[38] “Force measurement, piezoelectric force transducer: 5 rules for installation and mounting.” https://www.hbm.com/en/3212/piezoelectric_force_transducer_installation_and_mounting/. Accessed: 2015-10-25.

[39] “Force measurement, piezoelectric or strain gauge based force transducers.” https://www.hbm.com/en/3719/piezoelectric_or_strain_gauge_based_force_transducers/. Accessed: 2015-10-25.

[40] Physik Insturmente, *Technical Note, D-510 PISeca Single-Electrode Capacitive Sensor Probe*, 5 2011.

[41] Physik Insturmente, *PISeca Capacitive Sensors*, 1 2015.

[42] Polytec, *OFV-5000 Vibrometer Controller The Versatility in Vibration Measurement Datasheet*, 3 2016.

[43] K. U. Ingard and A. Akay, “On the vibration damping of a plate by means of a viscous fluid layer,” *Journal of Vibration, Acoustics, Stress and Reliability in Design*, vol. 109, pp. 178–184, 1987.

Appendix A

Technical drawings

All dimensions are given in technical drawings are in mm. Technical drawings of supporting parts for force transducer and capacitive sensor and technical drawings of both front view and back view are presented below. Even there are more than one force support part, only used part's technical drawing is given.

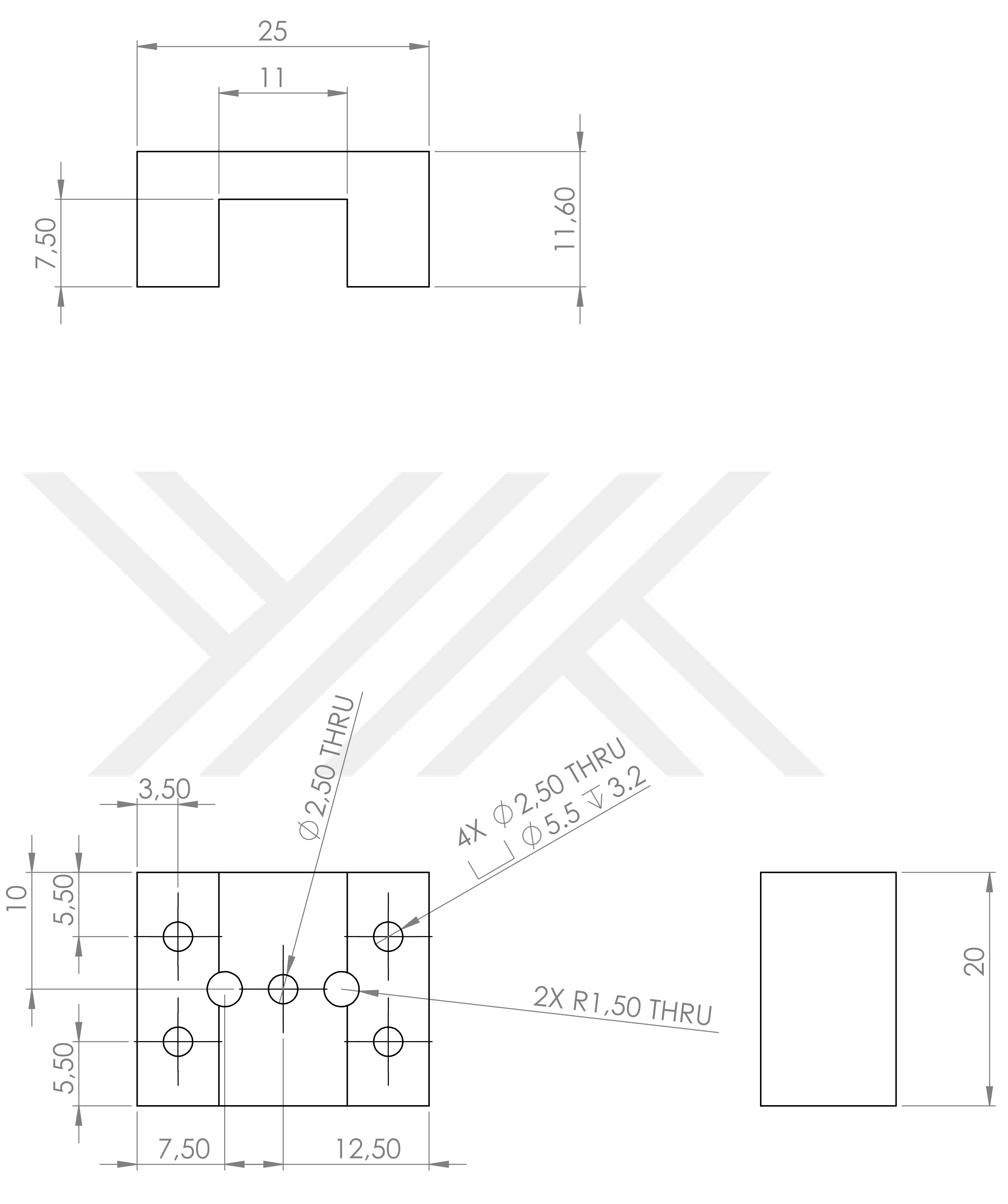

AKSİ BELİRTİLMEDİĞİ SÜRECE:
BOYUTLAR MİLİMETREDİR
YÜZEY CİLASI:
TOLERANSLAR:
DOĞRUSAL:
AÇISAL:

BİTİRME:

KESKİN KENARLARI PAHLAYIN VE KIRIN

TEKNİK RESMİ ÖLÇEKLENDİRME

REVİZYON

	İSİM	İMZA	TARİH
ÇİZEN			
DENET.			
ONAY.			
ÜRET.			
KALİTE			

BAŞLIK:

MALZEME:

RESİM NO. force_support_part8

A4

AĞIRLI:

ÖLÇEK:2:1

SAYFA 1 / 1

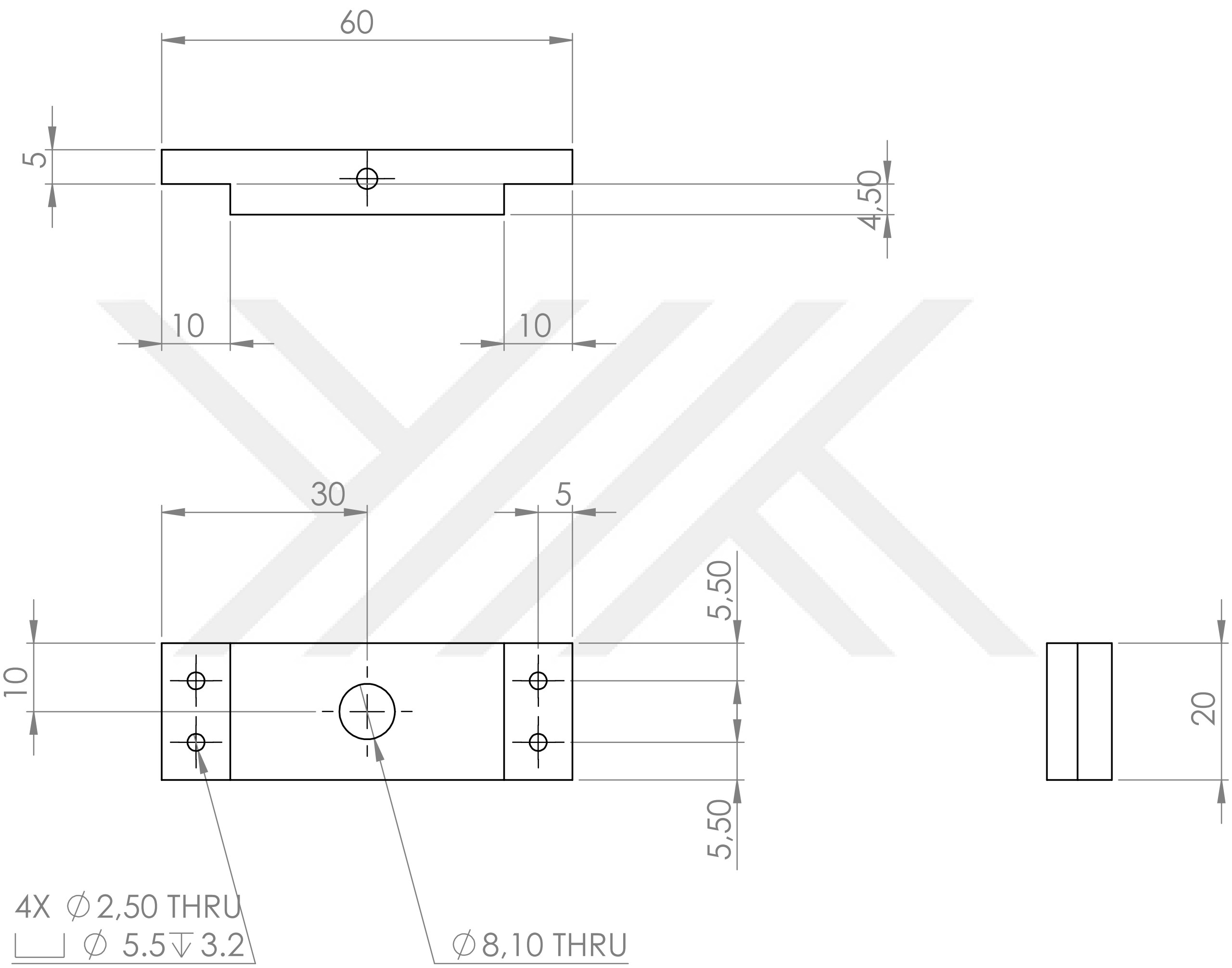

AKSİ BELİRTİLMEDİĞİ SÜRECE:
BOYUTLAR MİLİMETREDİR
YÜZEY CİLASI:
TOLERANSLAR:
DOĞRUSAL:
AÇISAL:

BİTİRME:

KESKİN KENARLARI PAHLAYIN VE KIRIN

TEKNİK RESMİ ÖLÇEKLENDİRME

REVİZYON

	İSİM	İMZA	TARİH
ÇİZEN			
DENET.			
ONAY.			
ÜRET.			
KALİTE			

BAŞLIK:

MALZEME:

RESİM NO. sensor_support_part5

A4

AĞIRLI:

ÖLÇEK:1:1

SAYFA 1 / 1

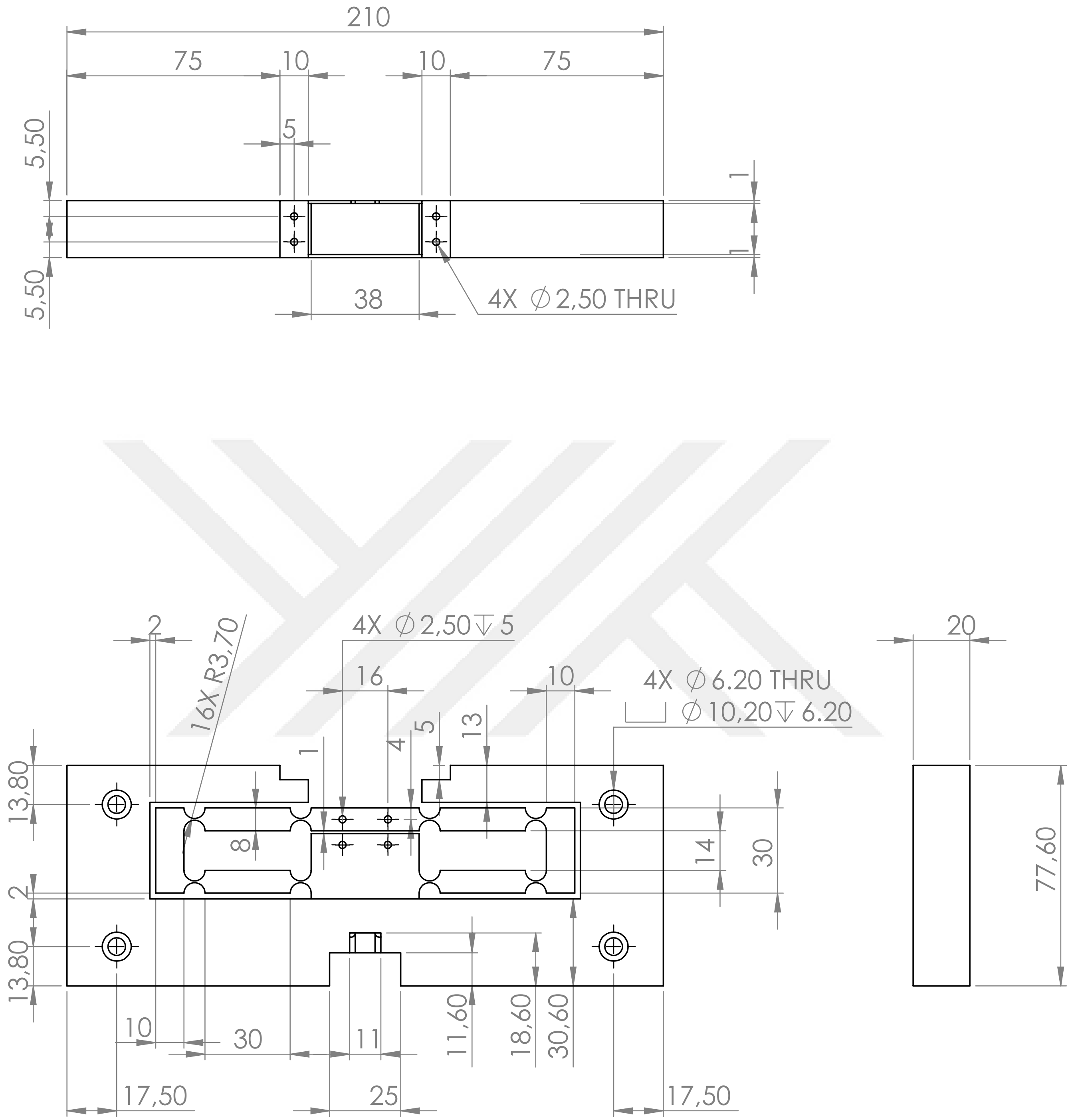

AKSİ BELİRTİLMEDİĞİ SÜRECE:
BOYUTLAR MİLİMETREDİR
YÜZEY CİLASI:
TOLERANSLAR:
DOĞRUSAL:
AÇISAL:

BİTİRME:

KESKİN KENARLARI PAHLAYIN VE KIRIN

TEKNİK RESMİ ÖLÇEKLENDİRME

REVİZYON

	İSİM	İMZA	TARİH		
ÇİZEN					
DENET.					
ONAY.					
ÜRET.					
KALİTE					

BAŞLIK:

MALZEME:

RESİM NO.

microtensile1_fv1_update10_manuf_d

A4

AĞIRLI:

ÖLÇEK:1:2

SAYFA 1 / 1

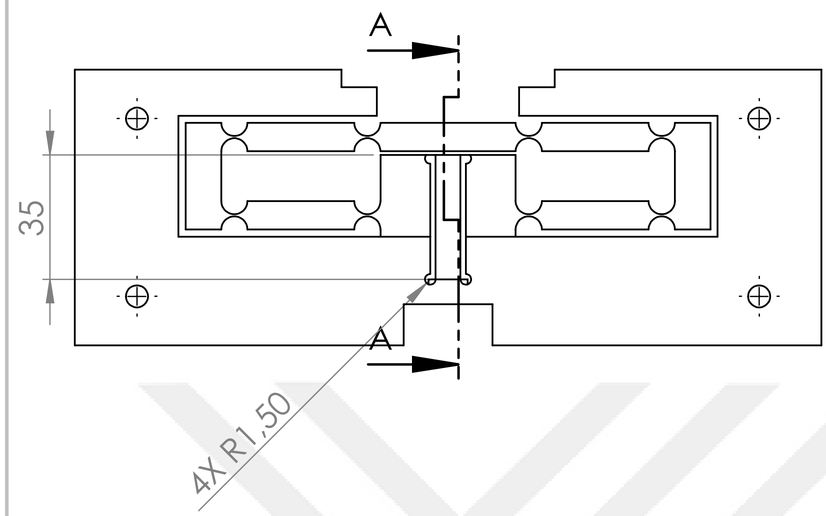

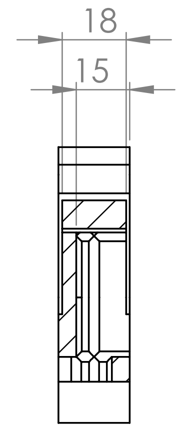

SECTION A-A

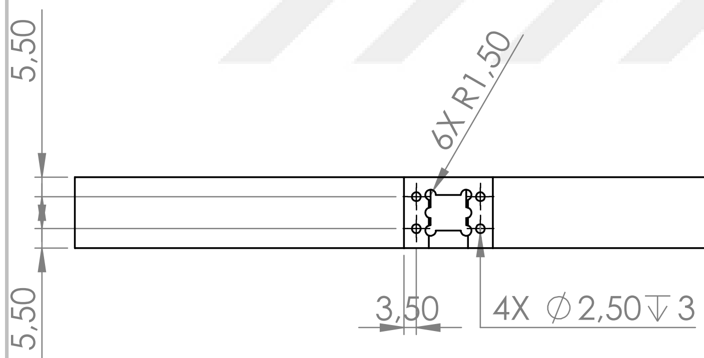

AKSİ BELİRTİLMEDİĞİ SÜRECE:
BOYUTLAR MİLİMETREDİR
YÜZEY CİLASI:
TOLERANSLAR:
DOĞRUSAL:
AÇISAL:

BİTİRME:

KESKİN KENARLARI PAHLAYIN VE KIRIN

TEKNİK RESMİ ÖLÇEKLENDİRME

REVİZYON

	İSİM	İMZA	TARİH		
ÇİZEN					
DENET.					
ONAY.					
ÜRET.					
KALİTE					

BAŞLIK:

MALZEME:

RESİM NO.

microtensile1_fv1_update10_manuf_dene

A4

AĞIRLI:

ÖLÇEK:1:2

SAYFA 1 / 1

Appendix B

MatLab Code

```
function [ max_force,min_force,max_disp,min_disp,index_max_force,
    index_min_force,index_max_disp,index_min_disp] =
    find_max_min_index(force,disp)
% find maximum and minimum values and corresponding indices of data
a=length(force);
c=length(disp);
m=1;
for k=(2:1:a-1)
   if (force(k)>force(k+1) && force(k)>force(k-1))
        max_force(m)=force(k);
        index_max_force(m)=k;
        m=m+1;
   end
end
m=1;
for g=(2:1:a-1)
   if (force(g)<force(g+1) && force(g)<force(g-1))
        min_force(m)=force(g);
        index_min_force(m)=g;
        m=m+1;
   end
end
m=1;
```

```
for b=(2:1:c-1)
   if (disp(b)>disp(b+1) && disp(b)>disp(b-1))
       max_disp(m)=disp(b);
       index_max_disp(m)=b;
       m=m+1;
   end
end
m=1;
for d=(2:1:c-1)
   if (disp(d)<disp(d+1) && disp(d)<disp(d-1))
       min_disp(m)=disp(d);
       index_min_disp(m)=d;
       m=m+1;
   end
end
end
```

```
function [force_vpp,disp_vpp] = Length_check( MaxF,MinF,MaxD,MinD)
% Calculates peak to peak values
if (length(MaxF)<length(MinF))
    force_vpp=MaxF-MinF(1:length(MaxF));
elseif (length(MaxF)>length(MinF))
    force_vpp=MaxF(1:length(MinF))-MinF;
else
    force_vpp=MaxF-MinF;
end

if (length(MaxD)<length(MinD))
    disp_vpp=MaxD-MinD(1:length(MaxD));
elseif (length(MaxD)>length(MinD))
    disp_vpp=MaxD(1:length(MinD))-MinD;
else
    disp_vpp=MaxD-MinD;
end

end
```

```
function [ Dc_force, Dc_disp ] = Dc_calculation(MaxF,MinF,MaxD,MinD)
```

```
% Calculate DC values

[MaxForce, MinForce, MaxDisp, MinDisp]=Same_length(MaxF,MinF,MaxD,
    MinD);
for m=1:1:length(MaxForce)
     Dc_force(m)=(MaxForce(m)+MinForce(m))/2;
end

for m=1:1:length(MaxDisp)
     Dc_disp(m)=(MaxDisp(m)+MinDisp(m))/2;
end

end
```